NASA

ION BEAMLET STEERING FOR TWO-GRID

ELECTROSTATIC THRUSTERS

PREPARED FOR

LEWIS RESEARCH CENTER

NATIONAL AERONAUTICS AND SPACE ADMINISTRATION

by

John M. Homa

Approved by

Paul J. Wilbur

July 1984

Department of Mechanical Engineeri
Colorado State University
Fort Collins, Colorado

15   1   1 RN/NASA-CR-174671
          DISPLAY 15/2/1
     84N31274*#   ISSUE 21   PAGE 3354   CATEGORY 20   RPT#: NASA-CR-174671 NAS
     1.26:174671   CNT#: NGR-06-002-112   84/07/00 83 PAGES   UNCLASSIFIED
     DOCUMENT
UTTL: Ion beamlet steering for two-grid electrostatic thrusters   TLSP: M.S.
     Thesis
AUTH: A/HOMA, J. M.
CORP: Colorado State Univ., Fort Collins.   CSS: (Dept. of Mechanical
     Engineering.)   AVAIL.NTIS   SAP: HC A05/MF A01
MAJS: /*DEFLECTION/*DIVERGENCE/*ELECTROSTATIC ENGINES/*ION BEAMS/*STEERING/*TUBE
     GRIDS
MINS: / DESIGN ANALYSIS/ EROSION/ IMPINGEMENT/ LATERAL CONTROL/ PERFORMANCE
     PREDICTION
ABA: M.A.C.

ABS: An experimental study of ion beamlet steering in which the direction of
     beamlets emitted from a two grid aperture system is controlled by relative
     translation of the grids, is described. The results can be used to design
     electrostatic accelerating devices for which the direction and focus of
     emerging beamlets are important. Deflection and divergence angle data are
     presented for two grid systems as a function of the relative lateral
     displacement of the holes in these grids. At large displacements,
     accelerator grid impingements become excessive and this determines the
     maximum allowable displacement and as a result the useful range of beamlet
ENTER:

1. Report No. NASA CR 174671	2. Government Accession No.	3. Recipient's Catalog No.
4. Title and Subtitle ION BEAMLET STEERING FOR TWO-GRID ELECTROSTATIC THRUSTERS		5. Report Date July 1984
		6. Performing Organization Code
7. Author(s) John M. Homa Paul J. Wilbur		8. Performing Organization Report No.
		10. Work Unit No.
9. Performing Organization Name and Address Department of Mechanical Engineering Colorado State University Fort Collins, Colorado 80523		11. Contract or Grant No. NGR-06-002-112
		13. Type of Report and Period Covered
12. Sponsoring Agency Name and Address		14. Sponsoring Agency Code

16. Abstract

An experimental study of ion beamlet steering in which the direction of beamlets emitted from a two-grid aperture system is controlled by relative translation of the grids, is described. The results can be used to design electrostatic accelerating devices for which the direction and focus of emerging beamlets are important. Deflection and divergence angle data are presented for two-grid systems as a function of the relative lateral displacement of the holes in these grids. At large displacements, accelerator grid impingements become excessive and this determines the maximum allowable displacement and as a result the useful range of beamlet deflection. Beamlet deflection is shown to vary linearly with grid offset angle over this range. Values of deflection-to-offset angle ratio and useful range of deflection are given as functions of grid-hole geometry, normalized perveance level, and accelerating voltage levels. The divergence of the beamlets is found to be unaffected by deflection over the useful range of beamlet deflection. The grids of a typical dished-grid ion thruster are examined to determine the effects of thermally induced grid distortion and prescribed offsets of grid hole centerlines on the characteristics of the emerging beamlets. The results are used to determine the region on the grid surface where ion beamlet deflections exceed the useful range. Over this region high accelerator grid impingement currents and rapid grid erosion are predicted.

17. Key Words (Suggested by Author(s)) Electrostatic Thruster Ion Optics	18. Distribution Statement Unclassified - Unlimited

19. Security Classif. (of this report) Unclassified	20. Security Classif. (of this page) Unclassified	21. No. of Pages 76	22. Price*

* For sale by the National Technical Information Service, Springfield, Virginia 22161

N84-31274#

TABLE OF CONTENTS

LIST OF FIGURES

NOMENCLATURE

d_a accelerator grid hole diameter

d_s screen grid hole diameter

E_1 electric field strength estimate, acceleration region

E_2 electric field strength estimate, deceleration region

E_r radial electric field strength

E_z axial electric field strength

f thin lens focal length

F_S open area fraction of screen grid

h dish depth of grids cold

j beam current density

J beam current per hole

ℓ Child's law acceleration length

ℓ_d deceleration length

ℓ_e' effective acceleration length

ℓ_g grid separation distance

m_i ion mass

NP/H   normalized perveance per hole

q charge

R net-to-total acceleration voltage ratio

r radial distance

Nomenclature (Continued)

t_a accelerator grid thickness

t_s screen grid thickness

V voltage

V_o axial voltage difference

V_N net accelerating voltage

V_T total accelerating voltage

v_i ion velocity

z axial distance

α beamlet divergence half-angle

β beamlet deflection angle

β_u useful beamlet deflection range

δ grid offset angle

δ_u useful grid offset angle range

ε_o free space permittivity

θ angle between thruster axis and normal to dished-grid surface

κ fractional change in accelerator grid hole spacing

λ relative grid axis displacement

I. INTRODUCTION

Ion sources are designed to produce directed beams of ions which can be used to propel spacecraft or in ground-based applications in which ion beams perform many material processing operations. An ion source, one of which is shown schematically in Fig. 1, consists of a discharge chamber and an electrostatic ion acceleration system. The ions are produced in the discharge chamber and then passed through the acceleration system where a collimated beam of ions with a desired exit velocity is produced. Electrons are then added to the beam to maintain a charge balance. This study is concerned with the acceleration system, therefore the processes involved in ion production will not be considered here. For the electrostatic ion acceleration used here, a pair of grids is attached to one end of the discharge chamber. The screen grid (Fig. 1) is kept at a positive potential with respect to ground, and the accelerator grid is biased negative of ground. A positively charged ion in the discharge chamber which drifts into the region between the grids is accelerated by the electric field that exists there. The ions passing through one pair of screen and accelerator grid holes form a pattern which is known as a beamlet as shown in Fig. 1. The beamlets tend to diverge, producing ion trajectories which are not parallel with the thrust axis. The extent to which the beamlets diverge is dependent on system parameters such as the relative sizes of the screen and accelerator grid holes, the separation distance between the grids, and the applied voltage between the grids.
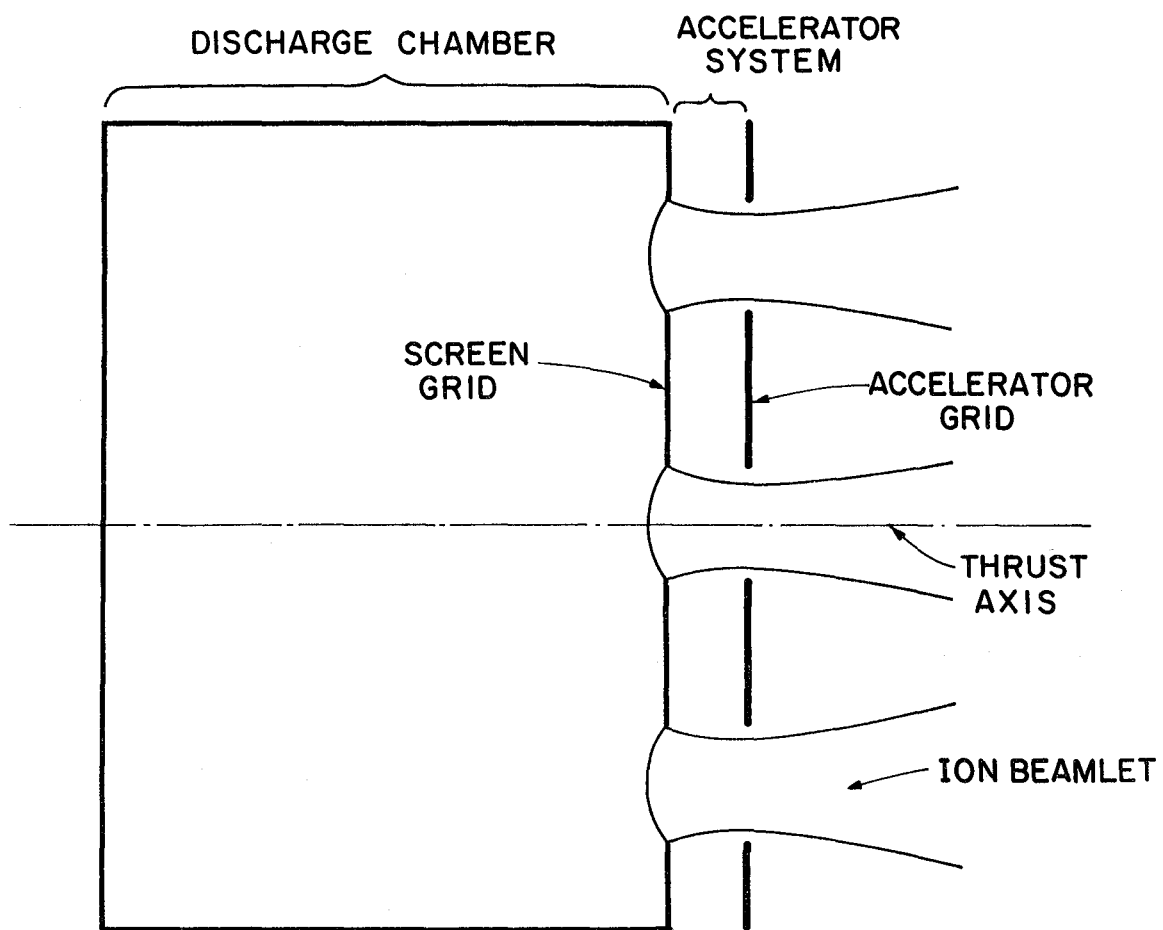
Figure 1. Ion Source Schematic

This study will investigate the process known as beamlet steering whereby the beamlets are re-directed with respect to the thruster axis. One method of accomplishing this is by translating one grid with respect to the other. In Fig. 1, for example, a vertical movement of the accelerator grid results in the mis-alignment of the axes of the screen and accelerator grid holes. The resulting non-symmetrical electric field configuration re-directs each beamlet to make an angle with the thruster axis. This study will determine the relationship between ion source operating parameters and the resulting characteristics of the vectored beamlets. The results will be useful in the design of ion sources in which the entire ion beam is to be vectored,[1] the individual beamlets are to be focused into some predefined pattern downstream,[2] or individual beamlets must be re-directed to compensate for a non-planar grid geometry. This last situation is encountered when the screen and accelerator grids are formed into a dished or curved shape. The beamlets must then be re-directed relative to the hole axis if they are to emerge parallel to the thrust axis.

Grid system characteristics have been studied previously by Aston[3,4] for cases in which screen-accelerator grid hole axes were aligned. The present study involves grid systems for which the grid hole axes are not aligned, and the beamlets are therefore vectored. Beamlet characteristics for both cases will be compared and the relationship between grid translation and beamlet vectoring will be determined for various grid configurations.

II. BACKGROUND

Grid Operation

Figure 2a depicts one pair of apertures from a grid set like the
one shown in Fig. 1. In this case the accelerator grid hole axis is
displaced a distance λ relative to the axis of the screen grid hole.
As a consequence the ion beamlet undergoes a deflection in the direc-
tion opposite to the accelerator grid translation through an angle
β with respect to the screen grid centerline. The deflected beamlet
also diverges with a half-angle α measured relative to the deflected
beamlet centerline. Figure 2a also illustrates pertinent grid dimen-
sions including screen and accelerator grid aperture diameters (d_s and
d_a), grid thicknesses (t_s and t_a) and the grid separation distance
(ℓ_g). The grid offset angle δ also shown in Fig. 2a is defined in
terms of the relative grid displacement λ by the equation:

$$\delta = \tan^{-1}\left(\frac{\lambda}{\ell_g + t_s}\right) \quad . \tag{1}$$

Figure 2b shows the typical variation of electrical potential with
axial position for the two-grid aperture configuration of Fig. 2a. The
discharge chamber plasma composed of positive ions and electrons is
biased to a high positive potential, V_N. As an ion crosses the plasma
sheath interface of Figure 2a, it is accelerated through a total po-
tential, V_T, toward the accelerator grid plane. After passing through
the accelerator grid hole the ion is then decelerated through a poten-
tial $|V_T|-V_N$. This potential barrier is necessary to prevent electrons

SCREEN
GRID

ACCEL
GRID

ACCEL GRID
HOLE AXIS

NEUT. PLANE

PLASMA
SHEATH

λ

d_a

δ

d_s

β

SCREEN GRID
HOLE AXIS

α

t_s

ℓ_g

t_a

δ = GRID OFFSET ANGLE
α = BEAM DIVERGENCE ANGLE
β = BEAM DEFLECTION ANGLE

a. BEAMLET NOMENCLATURE

ELECTRICAL POTENTIAL

V_N

V_T

ON BEAMLET
CENTERLINE

POSITION

THROUGH GRID WEBBING
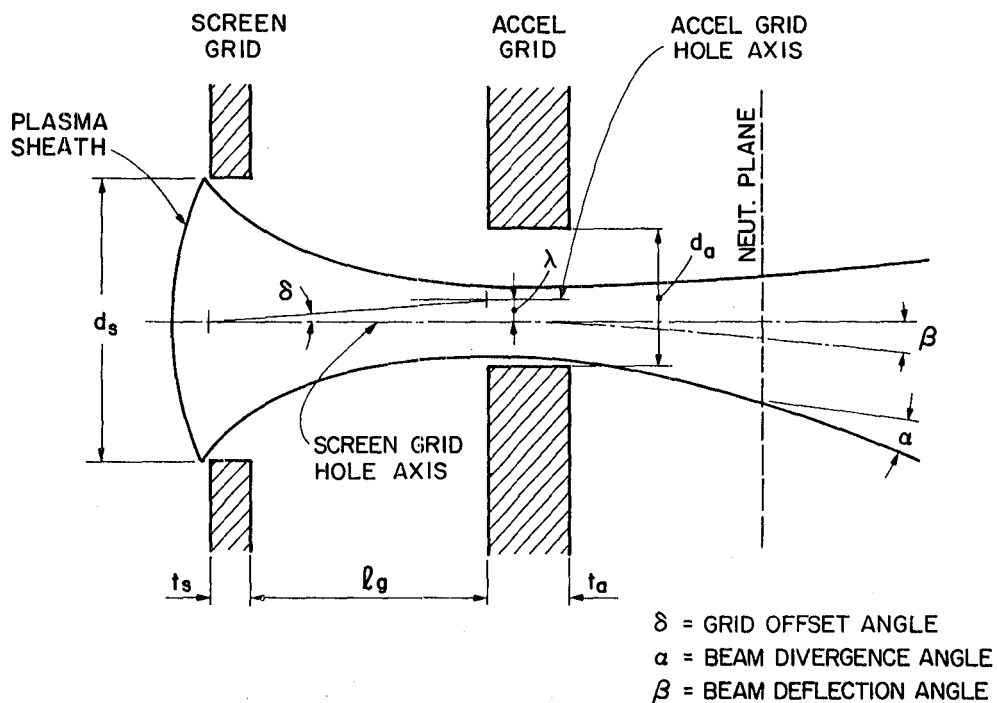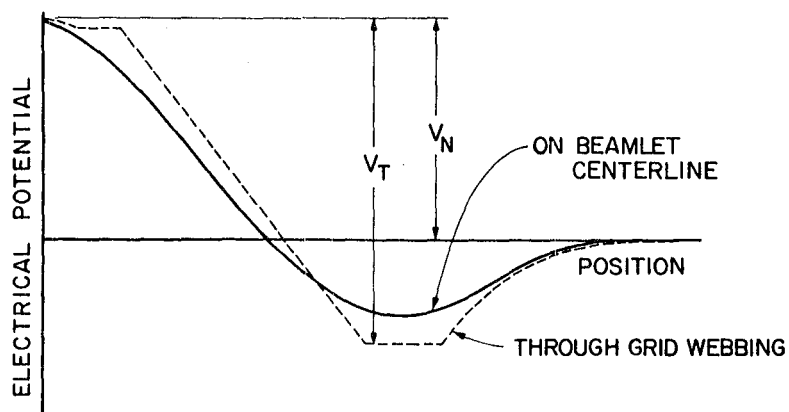
b. POTENTIAL PROFILE

Figure 2. Beamlet Nomenclature and Potential Variation

downstream of the grids from backstreaming through the grids. The ion
reaches ground potential with a final velocity which corresponds to the
net potential V_N :

$$v_i = \left(\frac{2qV_N}{m_i} \right)^{\frac{1}{2}} , \qquad (2)$$

where v_i is the ion velocity, q is the charge of the ion, and m_i is the
mass of the ion. The dotted line in Fig. 2b indicates the potential
variation through the grid webbing while the solid line shows the actual
potential variation for an ion which traverses the beamlet centerline.
When the trajectories of many ions are traced through the potential
variations they form the beamlet depicted in Fig. 2a. Most of the ions
pass through the accelerator grid hole; however, those that strike the
accelerator grid make up the accelerator grid impingement current.

The ratio of net accelerating voltage to total voltage is an im-
portant operating parameter affecting the deflection and divergence of
beamlets. This ratio, designated as the R-value is defined as:

$$R = \frac{V_N}{V_T} . \qquad (3)$$

An analysis of a one-dimensional ion current flow between parallel
plates shows that the current density of the extracted ions is limited
by an increase in the space charge density in the intervening gap. For an ion
of mass m_i and charge q, this extraction limit, known as the Child's law
current density limit,[5] is expressed as:

$$j = \frac{4}{9} \epsilon_0 \left(\frac{2q}{m_i} \right)^{1/2} \frac{V^{3/2}}{\ell^2} \qquad (4)$$

where j is the maximum current density that can be drawn between parallel plates, V is the potential applied between the plates separated by a distance ℓ and ε_0 is the permittivity of free space. The situation in which an ion current is extracted through a set of grid holes like those shown in Fig. 2a is also limited by space charge phenomena; however, this case is not one-dimensional. The one-dimensional model described above can be used to approximate this case if a value for the actual two-dimensional acceleration length can be approximated and substituted for ℓ in Eq. (4). The effective acceleration length chosen for this purpose is the one from the plasma sheath to the intersection of the screen hole centerline and the upstream surface of the accelerator grid. This length is given by:

$$\ell_e' = [(\ell_g + t_s)^2 + \frac{d_s^2}{4}]^{1/2} \ . \tag{5}$$

Using the total accelerating voltage V_T from Fig. 2b and the above acceleration length, the current density limit expression becomes:

$$j = \frac{4}{9} \varepsilon_0 \ (\frac{2q}{m_i})^{1/2} \ \frac{V_T^{3/2}}{\ell_e'^2} \ . \tag{6}$$

If one substitutes the current per hole J and the area of a screen hole for the current density, Eq. (6) becomes:

$$J = \frac{\pi}{9} \varepsilon_0 \ (\frac{2q}{m_i})^{1/2} (\frac{d_s}{\ell_e'})^2 \ V_T^{3/2} \ . \tag{7}$$

By arranging the physical constants on one side of the equation a normalized current per hole quantity known as normalized perveance per

hole is defined:

$$NP/H = \frac{J}{V_T^{3/2}} \left(\frac{\ell'_e}{d_s}\right)^2 = \frac{\pi}{9} \varepsilon_0 \left(\frac{2q}{m_i}\right)^{1/2} \quad . \tag{8}$$

For the singly charged argon ions used in this study, the normalized
perveance per hole based on a true one-dimensional acceleration process
is 6.8×10^{-9} $A/V^{3/2}$ or 6.8 nanopervs per hole. This should also repre-
sent an approximate limit for the two-dimensional case under considera-
tion here. The normalized perveance per hole represents then a properly
normalized parameter that can be used to compare the performance between
grids operating with various geometries and at various operating condi-
tions. By using a measured current per hole one can calculate a NP/H
value. Using this quantity, the performance of a particular grid set
can be compared to the theoretical limit as well as to the performance
of a variety of grid sets with different geometries and accelerating
voltages.

Linear Optics Theory

Linear optics theory[6,7] can be used to predict the beamlet deflec-
tion, β, as a linear function of the grid displacement, λ. The theory
is based on a two-dimensional solution to Laplace's equation, hence it
does not take into account the charge density effects on the potential
field. The following development of linear optics theory is useful
however, to illustrate the basic physics of the ion acceleration process
and the trends induced in beamlet deflection results when various
parameters are changed. Ion optics is somewhat analogous to light
optics, in that an ion passing through a distorted electric field is
deflected in a manner similiar to a light ray passing between materials

with different indices of refraction. It is noteworthy however that the path of the ion changes continuously as opposed to the discrete deflection of a light ray. The distorted field surrounding a grid aperture behaves in a manner similiar to a curved lens surface and has a focal length associated with it. The accelerator aperture of a two-grid system can be approximated as a thin lens with a focal length f, as shown in Fig. 3. A thin lens is one for which the thickness of the aperture is small in comparison with the focal length. Once the focal length for a given configuration is determined the beamlet deflection can be estimated. In order to determine the expression for the focal length, an equation for the motion of an ion through the potential field must be found. The general time-dependent equations of motion in two-dimensional cylindrical coordinates are:

$$\frac{d^2r}{dt^2} = \frac{q}{m_i} E_r (r,z) \tag{9}$$

$$\frac{d^2z}{dt^2} = \frac{q}{m_i} E_z (r,z) \tag{10}$$

where E_r is the electric field strength in the radial direction and E_z is the electric field in the axial direction. In this theoretical development, the ions begin with a zero initial velocity at a reference potential of zero volts. By combining these with the conservation of energy equation for ions:

$$\frac{m_i}{2} [(\frac{dr}{dt})^2 + (\frac{dz}{dt})^2] = -q \, V(r,z) \tag{11}$$
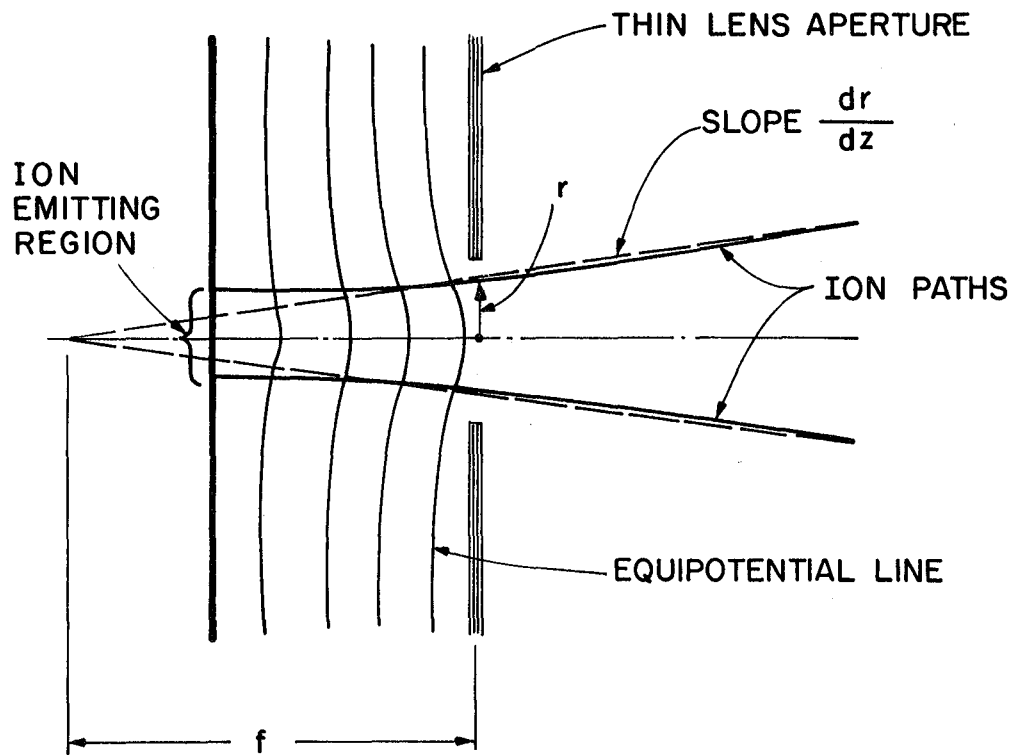
Figure 3. Cross-sectional View of an Axisymmetric Thin Lens Aperture

an expression for the ion path is obtained in terms of r, z, and the potential field:[*]

$$2 V \frac{d^2 r}{dz^2} = (E_z \frac{dr}{dz} - E_r) (1 + (\frac{dr}{dz})^2) \qquad (12)$$

For ion thruster applications, ions generally approach the lens on trajectories that make angles with the hole centerline that are small. In this case, the $(\frac{dr}{dz})^2$ term is negligible. The potential and potential field terms of Eq. (12) can be replaced by a power series solution to Laplace's equation. This expansion gives the potential anywhere in the field in terms of the axial potential, i.e. $V_0(0,z)$. For the ions which make small angles with respect to the axis, only the first term of the power series expansion is needed. Making these substitutions one obtains:

$$\frac{d^2 r}{dz^2} + \frac{V_0'}{2V_0} \frac{dr}{dz} + \frac{rV_0''}{4V_0} = 0 \qquad (13)$$

where the primes denote differentiation with respect to z. As suggested

---

* This expression shows that the charge and mass terms of Eqs. 9, 10, and 11 have cancelled out and therefore the ion paths should be the same for propellants with different charge-to-mass ratios. A previous study[4] has shown that operation with different propellants did not substantially change the beamlet divergence characteristics. The results of the present study should therefore be generally applicable to a variety of propellants. Section V. of this study contains additional information concerning propellant changes.

by Fig. 3, the focal length is defined by the geometrical relationship between the radial position of an ion trajectory at the aperture and the slope of the straight line trajectory in the field-free region beyond the lens. This is given by:

$$\left(\frac{dr}{dz}\right)_2 = \frac{-r}{f_2} \tag{14}$$

The negative sign indicates that for a positive slope, (an ion diverging from the axis) a negative focal length results (a divergent lens). By integrating Eq. (13) and combining it with Eq. (14) an expression for the focal length is obtained:

$$\frac{1}{f} = \frac{V_{0_2}' - V_{0_1}'}{4 V_{0_2}} + \frac{1}{8 (V_{0_2})^{1/2}} \int_{z_1}^{z_2} \frac{(V_0')^2}{V_0^{3/2}} \, dz \tag{15}$$

where the subscripts 1 and 2 refer to the upstream and downstream sides of the accelerator grid, respectively, and potentials are measured relative to the ion emitting surface. In the present case for which the potential gradients are large, the second term on the right-hand side is not significant[7] and the equation for the focal length becomes:

$$f = \frac{4 V_T}{E_1 - E_2} \tag{16}$$

where V_T is the potential of the accelerator grid with respect to the screen grid and E_1, E_2 are the electric fields on the acceleration (upstream) and deceleration (downstream) sides of the accelerator grid, respectively. For aligned apertures the beamlet emerges such that the

current density is distributed symmetrically about the aperture center-
line. When the accelerator aperture is displaced a distance λ, the
beamlet emerges about a line which makes an angle β with the centerline.
This beamlet deflection angle, β is given by:[6]

$$\beta = \frac{\lambda}{f} \tag{17}$$

where λ is the relative grid displacement. Equation (17) is valid for
small values of the angle β . Substituting the expression for focal
length into Eq. (17) gives:

$$\beta = \frac{\lambda(E_1 - E_2)}{4 \, V_T} \quad . \tag{18}$$

When the potential gradient upstream of the accelerator grid is approxi-
mated as the total accelerating voltage divided by the grid separation
distance, i.e., space charge effects are neglected, Eq. (18) becomes:

$$\beta = \frac{-\lambda}{4\ell_g} \left(1 - \frac{E_2}{E_1}\right) \quad . \tag{19}$$

Since E_2 and E_1 are of opposite sign, it can be seen from the above
equation that the beamlet deflection occurs in the direction opposite
to the displacement of the accelerator grid. For the situation in
which the deceleration potential is small (high R-values), $|E_2| \ll |E_1|$
the equation for beamlet deflection simplifies further to:

$$\beta = \frac{-\lambda}{4\ell_g} \quad (\beta \text{ in radians}), \tag{20}$$

or

$$\beta = -14.3 \, \frac{\lambda}{\ell_g} \quad (\beta \text{ in degrees}). \tag{21}$$

For operation at the lower R-values, which are also of interest in ion thruster applications, the deceleration field E_2 is significant. In this case an estimate of the deceleration potential field, E_2 must be found to use in Eq. (19). The distance between the accelerator grid and the downstream neutralization plane is needed to make this estimate. For a two-grid system this is not generally known; however, an estimate for this deceleration length, ℓ_d has been given by Kaufman[5] as:

$$\ell_d = \ell_e \left[(1 + 3R^{\frac{1}{2}} - 4R^{3/2})/F_s (j/j_{CL})\right]^{\frac{1}{2}} \qquad (22)$$

where F_s is the screen grid open area fraction, and j/j_{CL} is the ratio of open area current density to the Child's law current density. The Kaufman acceleration length, ℓ_e is defined as:

$$\ell_e = \left(\ell_g^2 + \frac{d_s^2}{4}\right)^{\frac{1}{2}} . \qquad (23)$$

By dividing the deceleration potential, $|V_T|-V_N$ by the estimated deceleration length, ℓ_d a rough estimate of the potential gradient is determined. For a typical case in this study with $V_T = 600$ volts, $R = 0.5$, and $\ell_g = 1.02$ mm, the factor $(1 - \frac{E_2}{E_1})$ from Eq. (19) is 1.14. The result is a 14% increase in beamlet deflection angle for a given grid displacement. This demonstrates that the deceleration potential gradient increases beamlet deflection when operation occurs at a moderate net-to-total accelerating voltage ratio.

III. APPARATUS AND PROCEDURE

Apparatus

The beamlet vectoring study has been conducted on an 8 cm diameter electron bombardment ion source. The discharge chamber plasma is produced by bombarding neutral argon propellant atoms with energetic electrons. These electrons are contained within the discharge chamber by a mildly divergent axial magnetic field. Argon was selected as the propellant due to the high fraction of singly charged ions produced in the discharge chamber and its nonreactivity. The extraction grids have been masked down so ions are extracted only through a central region of the grids having ~ 1 cm^2 area. This ensures that uniform plasma properties exist across this 1 cm^2 region and hence a uniform beam is produced at the accelerator grid plane. Electrons are added to the beam downstream of the grids in order to maintain a charge balance. The thruster uses tungsten wire filaments for both the main and neutralizer cathodes.

The grids were fabricated from high density graphite sheets, since graphite has a relatively low sputter yield and is easy to machine. The screen hole diameter was selected to be 2.1 mm and the active region of the grid consisted of 19 of these apertures arranged in a hexagonal pattern with a center-to-center spacing of 2.5 mm. The accelerator grid hole diameter was varied but had the same center-to-center spacing as the screen grid. Mica insulating sheets were used to maintain the separation between the two grids. The test apparatus is designed so

the accelerator is held fixed and the screen grid can be translated along one axis during thruster operation by a mechanical system in the manner suggested by Fig. 4. The screen grid was selected as the translating grid, because such an arrangement facilitated grid spacing and accelerator grid alterations. Initial alignment of the grids was accomplished by using a magnifying lens to insure that as the screen grid was translated it passed through the aligned position.

The beam emerging from the grids is probed by a collection of molybdenum, flat plate Faraday probes each 1 cm^2 in area, arranged in the manner suggested in Fig. 4. Molybdenum was used as the probe sensing element because it has a low secondary electron emission coefficient. Twenty probes are situated along a horizontal line 14 cm downstream from the grids. In addition, a line of probes extends vertically downward from each end of the horizontal probe rake. By using these three probe rakes it is possible to intercept the full beam current profile over the complete range of grid translation. Since the beam has been neutralized immediately downstream of the grids, a screen is required in front of the probes. This screen which has a 70% open area fraction is biased 24 v negative relative to ground in order to reflect the neutralizer electrons. The true ion currents to the probe are computed by dividing by 0.70 to account for ion interception on the screen. In addition, the probes themselves are biased 18 v positive relative to ground to reflect low energy charge-exchange ions produced by collisions between neutral background atoms and beam ions downstream of the grids. The rake assembly is designed so it can be rotated in the manner suggested in Fig. 4 to facilitate rake axis alignment with the beam axis in the plane perpendicular to the direction of grid translation.

ELECTRON SHIELDING
SCREEN

FARADAY PROBE (typ.)

9.5 cm

HORIZONTAL
PROBE RAKE

VERTICAL
PROBE RAKES

14 cm

MECHANICAL
TRANSLATION
SYSTEM

ACCEL GRID

SCREEN GRID

8 cm Argon
ION
SOURCE

TO MICROMETER

RAKE ASSEMBLY ROTATION
TO FACILITATE ALIGNMENT
WITH BEAM

PROBE RAKE
ASSEMBLY

ION SOURCE

17
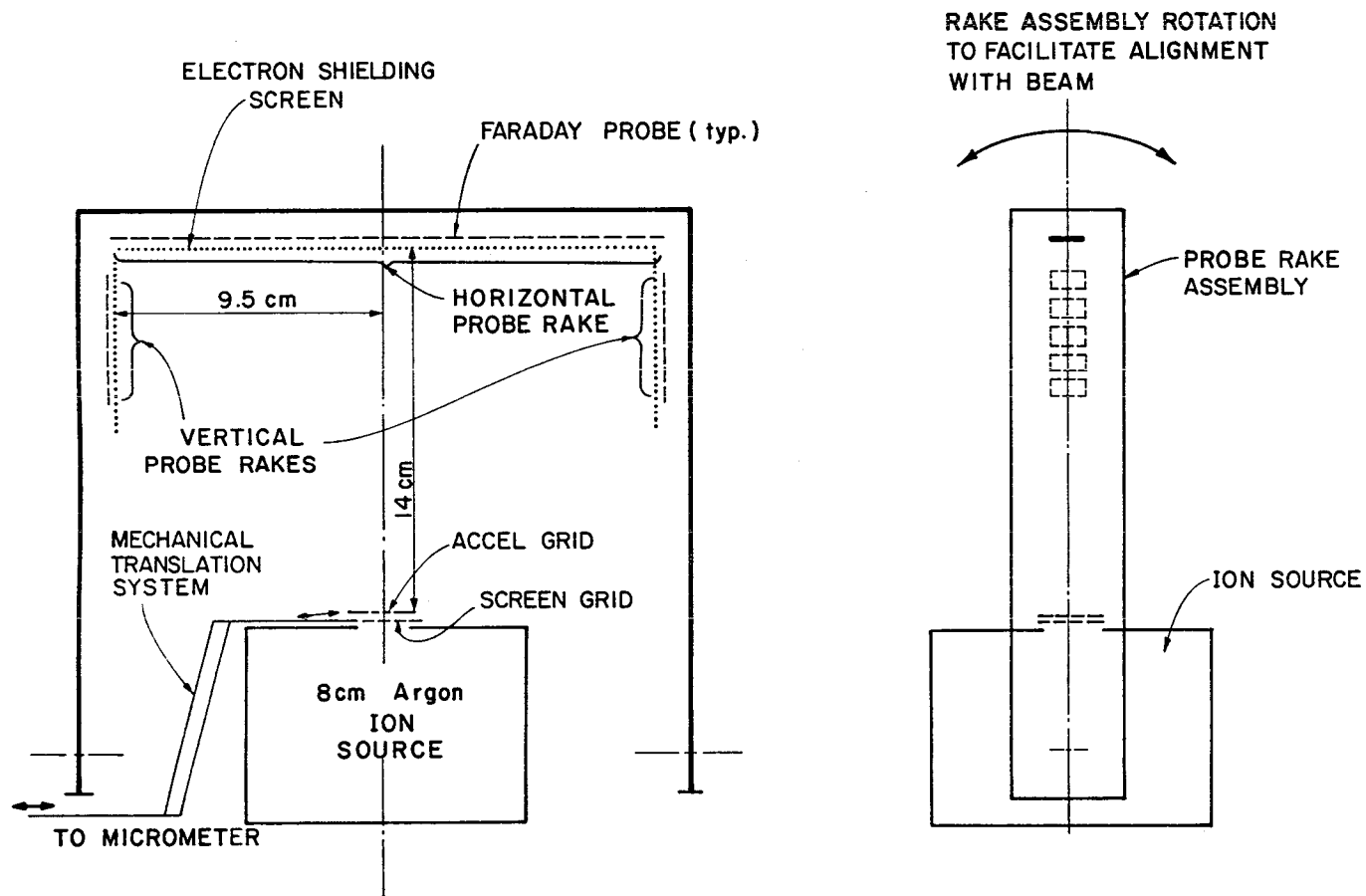
Figure 4. Deflecting Beamlet Test Apparatus

Procedure

In conducting these tests, stable ion source operation is established with the screen grid displaced to produce a substantial negative ion beam deflection. The ion beam is then probed using the Faraday probe rake system. The screen grid is displaced 0.05 mm and the beam is probed again. This process continues until the beam is displaced sufficiently positive so the accelerator grid impingement current reaches approximately 25% of the beam current. After this complete set of profiles has been recorded, the beam current and grid voltage are changed and the process is repeated. Since a grid displacement of 0.05 mm has been shown to produce measurable beam deflection, careful alignment of the grids in the direction perpendicular to the direction of grid translation and reduction of play in the movable grid are crucial to the generation of accurate data.

Beam current density profiles are analyzed using a computer routine. This routine first uses the current density data obtained from the thirty element probe rake to compute the current density profile on a circular arc located 17 cm from the grid center. From this profile the point of maximum current density is identified. An initial estimate of the deflection angle is then computed as the angle between the thruster axis and the line from the screen grid center through the point of maximum current density. Next the two segments of the current density profile on either side of the maximum are averaged and the total beam current is estimated by integrating this average profile for an assumed axi-symmetric distribution about the line of maximum current density. The line of assumed symmetry is then perturbed from the line of maximum current density and the integration is repeated. This leads

to a new value of integrated beam current. This process is repeated
until the line of assumed symmetry yields a minimum beam current. The
axis about which the beam current is a minimum is by definition the
centroidal axis of the beam current. The deflection angle is then the
angle between this beam axis and the thruster axis. The final beam cur-
rent obtained in the analysis is then compared to the measured beam cur-
rent to insure that they agree to within 5 to 10%. The divergence angle
(α in Fig. 2a) is computed as the half angle of the cone enclosing 95%
of the integrated beam current determined in the aforementioned
analysis. This definition of half angle is the same as the one used by
Aston[3,4] in the study of divergence characteristics of aligned grids.

Initially, current density data were collected manually by reading
a meter that could be switched to read each Faraday probe in the rake.
These results showed the linear relationship between the grid offset
angle (δ) and the deflection angle (β) predicted by Eq. (20), but, in-
consistencies were observed when data from various runs were compared.
It was determined that these inconsistencies were due in part at least
to variations in ion source operating conditions that occurred while
the probe currents were being read. In order to minimize this drift the
manual data collection was eliminated in favor of automated collection
using a data logger. Results obtained using the data logger have been
more reproducible and self-consistent.

In order to isolate the effects of various parametric changes to
be introduced in the experiment a standard grid geometry was selected
and then one grid parameter was varied while other parameters were held
at their standard value. The standard case selected is defined by the
following geometrical and operating conditions:

Screen hole diameter (d_s)	2.1 mm
Total accelerating voltage (V_T)	600 volts
Net-to-total accelerating voltage ratio (R)	0.70
Screen grid thickness ratio (t_s/d_s)	0.18
Accelerator grid thickness ratio (t_a/d_s)	0.37
Accelerator grid hole diameter ratio (d_a/d_s)	0.64
Grid separation ratio (ℓ_g/d_s)	0.49

As suggested by the above list, the geometrical grid parameters of Fig. 2a are normalized using the screen hole diameter, which was held constant at 2.1 mm for all tests. The range of variation of the parameters investigated in this study were:

Total accelerating voltage (V_T)	600 - 1100 volts
Net-to-total accelerating voltage ratio (R)	0.35 - 0.90
Screen grid thickness ratio (t_s/d_s)	0.18 - 0.37
Accelerator grid thickness ratio (t_a/d_s)	0.12 - 0.74
Accelerator grid hole dia. ratio (d_a/d_s)	0.64 - 1.00
Grid separation ratio (ℓ_g/d_s)	0.49 - 1.00

In addition, the discharge (anode) voltage was maintained at 40 v, which is high enough to assure efficient ionization and low enough so that the production of doubly charged ions is small. An argon flow rate of 10 mA equivalent was used throughout the experiments because it was sufficiently high to produce stable discharge chamber operation while being low enough to keep the charge exchange ion production less than one percent of the beam current. This argon flow rate resulted in a bell jar pressure in the range of 6 - 8 x 10^{-6} Torr.

IV. EXPERIMENTAL RESULTS AND DISCUSSION

A typical beam ion current density profile collected in the manner outlined in the previous section is shown in Fig. 5a. As this figure suggests, the profiles are relatively symmetrical and this symmetry is retained within the useful range of beam deflections. Using the information on this profile one can determine the beamlet divergence and deflection associated with this particular grid geometry and relative grid offset. A typical plot of deflection angle vs. grid offset angle obtained from many profiles like the one of Fig. 5a, but each at a different offset, is presented in Fig. 5b. This one is for the standard grid set operating at an R-value of 0.70 and a normalized perveance per hole (NP/H) of 1.02×10^{-9} A/V$^{3/2}$ where:

$$NP/H = \frac{J}{V_T^{3/2}} \left(\frac{\ell'_e}{d_s} \right)^2 . \qquad (24)$$

In this equation J is the ion current per hole, i.e. total measured beam current divided by the number of holes (19 in this case).

Figure 5b shows a linear relationship between deflection angle (β) and grid offset (δ) up to a grid offset angle of $\sim 15°$. This linear relationship is in agreement with elementary optical theory (Eq. (21)). The deflection angle at the onset of the non-linear behavior, where the beamlets begin to intercept the accelerator grid and prolonged operation is not possible, is designated β_u (for β useful) as suggested in Fig. 5b. The data shown in this figure is for the standard case accelerator grid

ARGON

$$\frac{t_s}{d_s} = 0.18 \qquad \frac{\ell_g}{d_s} = 0.49$$

$$\frac{t_a}{d_s} = 0.37 \qquad \frac{d_a}{d_s} = 0.64$$

$$V_T = 600\,V \qquad R = 0.7$$

$$NP/H = 1.02 \times 10^{-9}\ A/V^{3/2}$$

CURRENT DENSITY PEAK

PROFILE OFFSET

PROBE CURRENT ($\mu A/cm^2$)

PROBE DISTANCE (cm)

a. BEAM CURRENT DENSITY PROFILE

DEFLECTION ANGLE $[\beta]$ (deg)

β_u

GRID OFFSET ANGLE $[\delta]$ (deg)

δ_u
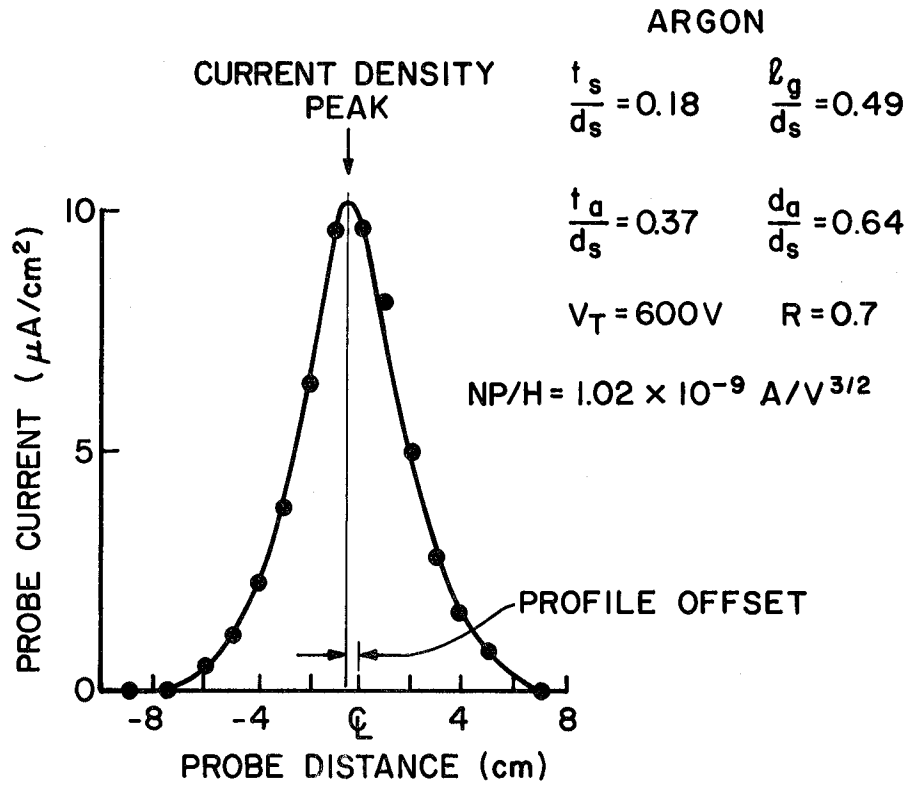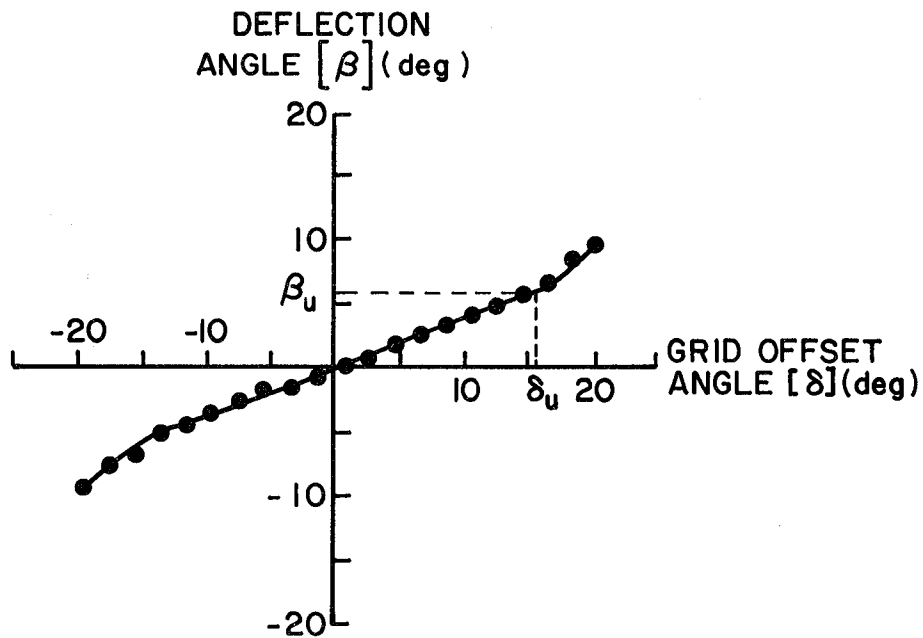
b. DEFLECTION CHARACTERISTIC

Figure 5. Typical Standard Grid Data, Beam Current Density Profile and Deflection Characteristics

hole diameter ratio of 0.64. At accelerator hole to screen hole diameter ratios near 1.00 the beam deflection beyond β_u levels off rather than increasing as shown in Fig. 5b, but the slope of the curve generally changes at this point. This change in the slope above the point where impingement begins to increase is probably related to the observation that the beam profiles become increasingly asymmetrical at high grid offset angles. It should be noted that the non-linear beam deflection always occurs at relatively high impingement levels which are outside of the normal thruster operating regime. It is therefore not necessary to characterize the beamlets above this point.

The experimental deflection characteristics illustrated in Fig. 5b can be compared with the theoretical relation expressed in Eq. (19). In Fig. 5b, the ratio of deflection angle to grid offset angle (β/δ) is equal to 0.43 over the linear region of beamlet deflection. An experimental correlation of the same form as the theoretical one given in Eq. (19) can be obtained from this data, namely:

$$\beta = -17.8 \frac{\lambda}{\ell_g} \quad (\text{ in degrees}) \tag{25}$$

The coefficient in this equation is not far from the theoretical value of 15.2°, obtained by substituting into Eq. (19) the estimates of the electric fields E_1 and E_2 developed in Section II. It is also in reasonable agreement with previously measured values.[8] As stated in Section II., Eq. (19) predicts an increase in the coefficient in this equation if the deceleration field E_2 is significant, as it should be for the data of Fig. 5 where the net-to-total accelerating voltage ratio (R) is less than unity. For the standard grid geometry data obtained at

net-to-total voltage ratios of 0.90 and 0.50 the experimental correlation values for Eq. (25) are 16.5° and 20.7°, respectively. This shows a clear trend of increase, as predicted by Eq. (19).

Typical divergence and impingement characteristics for the grid set of Fig. 5 are given in Fig. 6. It can be seen in Fig. 6a that the divergence angle (α) does not vary significantly over the useful range of grid offset angles where the impingement currents are acceptably low and operation would normally occur. With a larger accelerator grid hole diameter ratio (d_a/d_s) the divergence angle drops slightly from the value at a significant offset to a minimum at zero offset. Even in the worst case, however, the total variation in divergence angle over the useful range of grid offset angle was not observed to exceed two degrees. The rapid decrease in divergence angle apparent in Fig. 6a at large grid offset angles is probably due to interception of the most divergent ions from the beamlets by the accelerator grid. In Fig. 6b this rapid increase in accelerator grid ion (impingement) current is apparent and it defines the range of useful grid offset angles (δ_u). In order to quantify this range it is defined here rather arbitrarily as the grid offset angle at which the impingement current reaches 10% of the beam current. This sets the limit on the useful range of beam deflection (β_u) which is indicated on Fig. 5b. Using a collection of data like those shown in Figs. 5 and 6, one can define a group of parameters that characterize the optical behavior of deflected ion beamlets. The parameters that have been selected for use here are:

1. The useful ion beamlet deflection range (β_u)

2. The deflection-to-offset angle ratio in the useful range (β/δ)

3. Divergence angle in the useful range (α)

DIVERGENCE ANGLE, $[\alpha]$ (deg)

ARGON

$\dfrac{t_s}{d_s} = 0.18$ $\qquad$ $\dfrac{\ell_g}{d_s} = 0.49$

$\dfrac{t_a}{d_s} = 0.37$ $\qquad$ $\dfrac{d_a}{d_s} = 0.64$

$V_T = 600V$ $\qquad$ $R = 0.70$

$NP/H = 1.02 \times 10^{-9}$ A/V$^{3/2}$

20

15

10

5

-20 $\quad$ -10 $\quad$ 0 $\quad$ 10 $\quad$ 20

GRID OFFSET ANGLE $[\delta]$ (deg)

a. DIVERGENCE ANGLE DATA

IMPINGEMENT CURRENT (μA)

180

160

120

80

40

RANGE OF USEFUL GRID OFFSET (δ_u)

-20 $\quad$ -10 $\quad$ 0 $\quad$ 10 $\quad$ 20

GRID OFFSET ANGLE $[\delta]$ (deg)
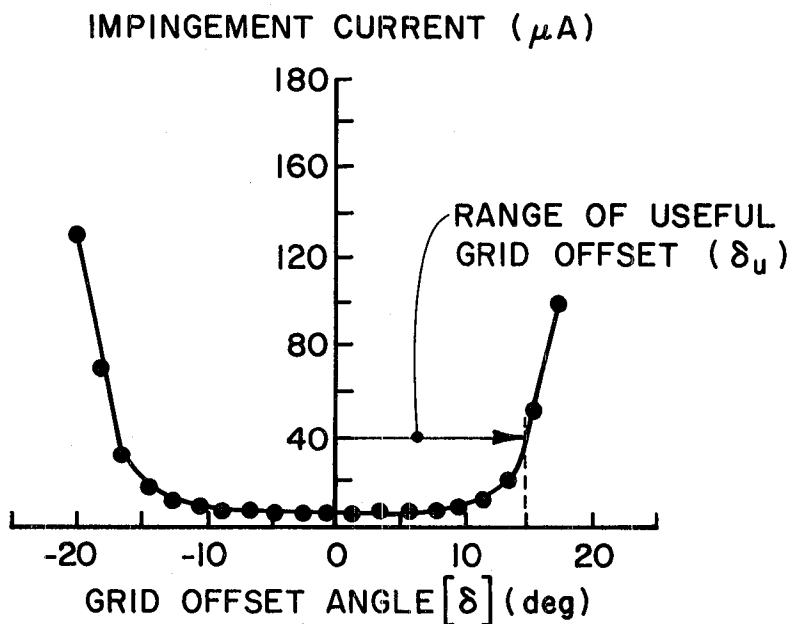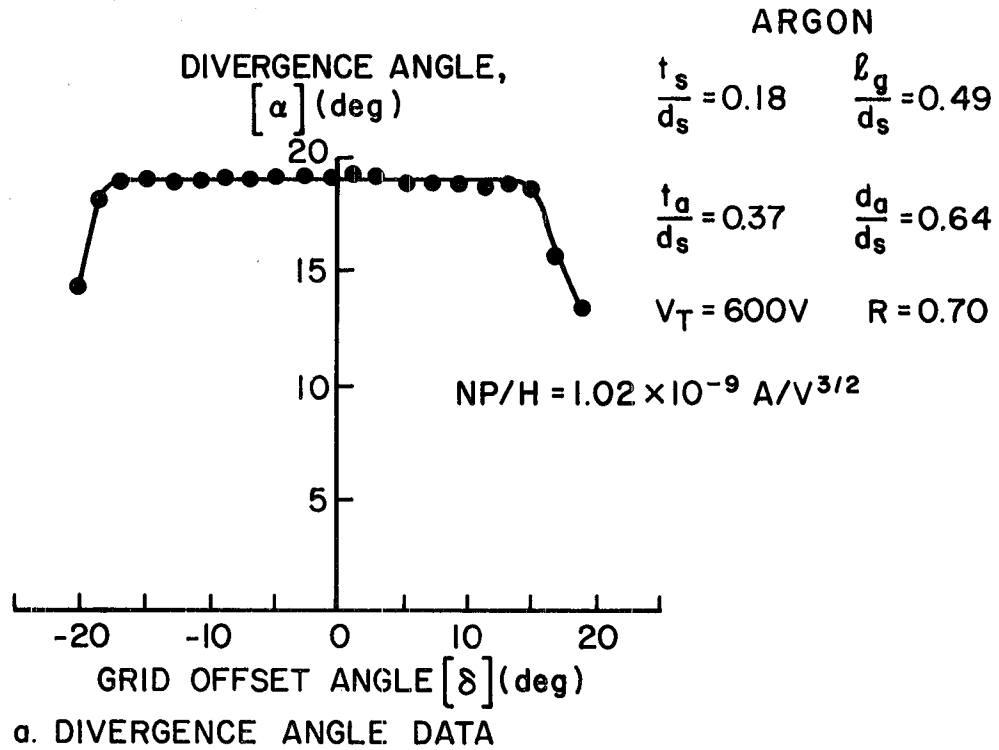
b. ACCELERATOR GRID IMPINGEMENT DATA

Figure 6. Typical Standard Grid Data, Divergence Angle and Accelerator Grid Impingement

It is noteworthy that the useful range of the grid offset angle (δ_u) is a function of both the geometrical parameters of the grids and the perveance at which they are operating. Figure 7 illustrates the effect of perveance on typical impingement current vs. grid offset angle plots. The two values of useful range of grid offset angle (δ_u) appropriate to the two levels of perveance are identified and they show that the limiting offset angle drops as the perveance is increased. This presumably occurs because the beamlet more nearly fills the accelerator grid aperture at the higher perveance level.

Effect of Grid Offset on Beamlet Divergence

The assumption that a single divergence angle (α) characterizes the beamlets over the range of useful deflection is supported by the results of Fig. 8, which show that the divergence angle is independent of grid offset angle over the full range of perveance. The divergence angle results also agree to with $\sim 2°$ with those obtained by Aston[3] using aligned grids. In comparing these results it should be noted that a slightly different definition of the effective ion acceleration length is used to compute the perveances.[9] The justification for using a different length here is discussed in Appendix A.

Figure 9 shows the effects of net-to-total voltage ratio (R) on beamlet divergence (α). The beamlet divergence angle is seen to be strongly dependent on the net-to-total voltage ratio. These typical curves again agree reasonably well with those obtained by Aston.[3]

Divergence curves showing the effects of other parameters investigated are similar to results obtained by Aston when account is taken for the new definition of acceleration length. Since Aston's work utilized
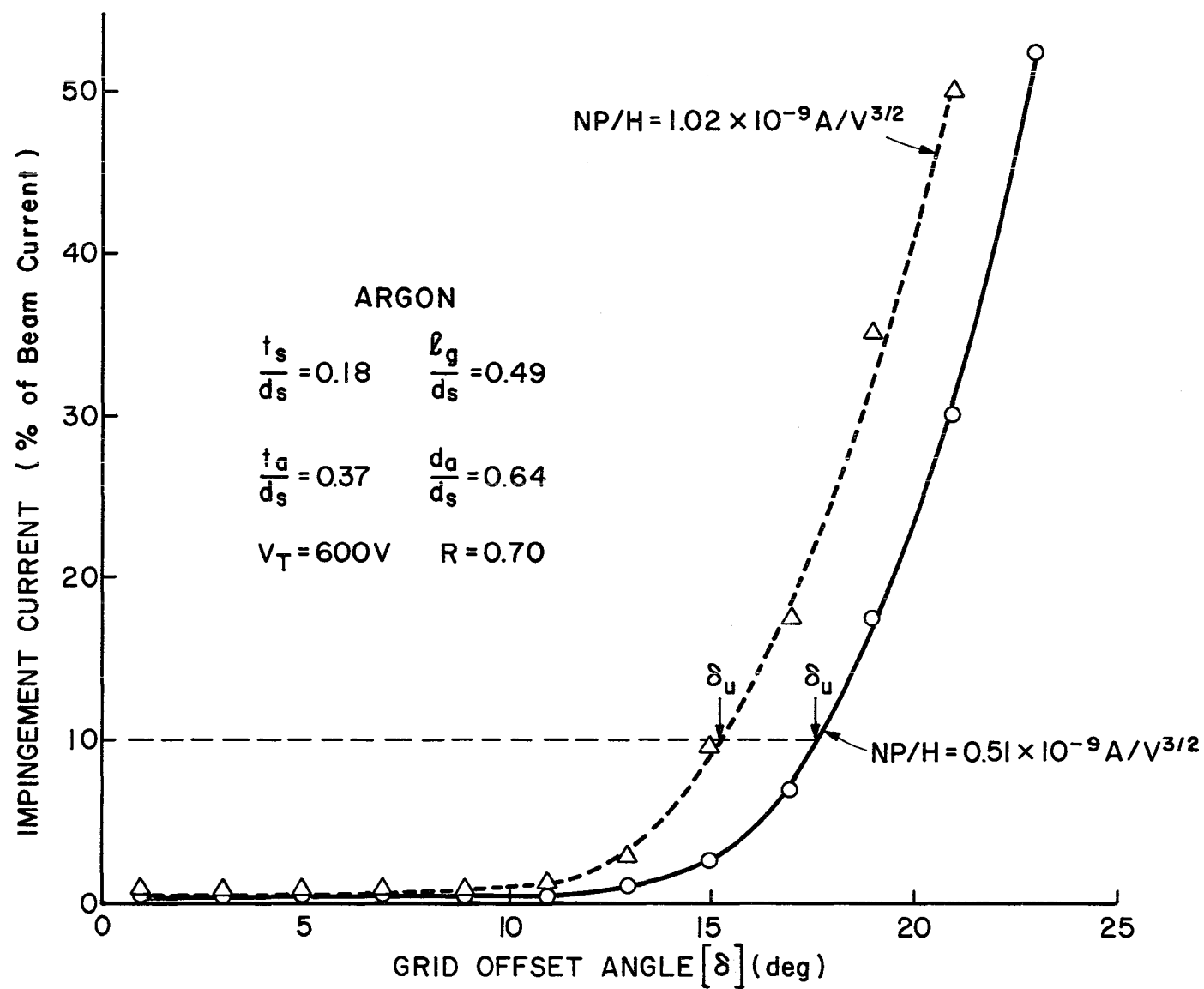
Figure 7.   Effect of Grid Offset on Impingement Current.
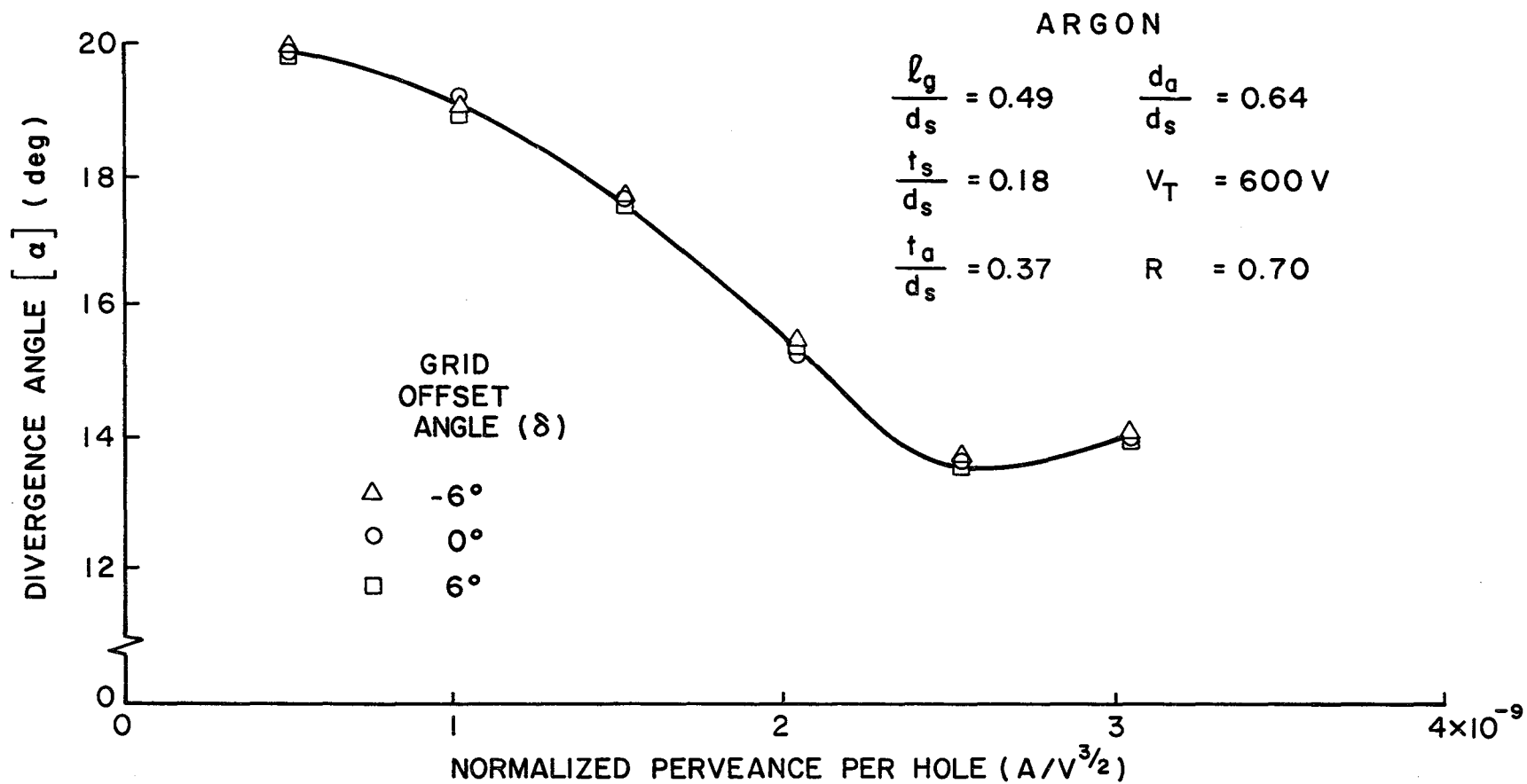
Figure 8.   Effect of Grid Offset on Beamlet Divergence
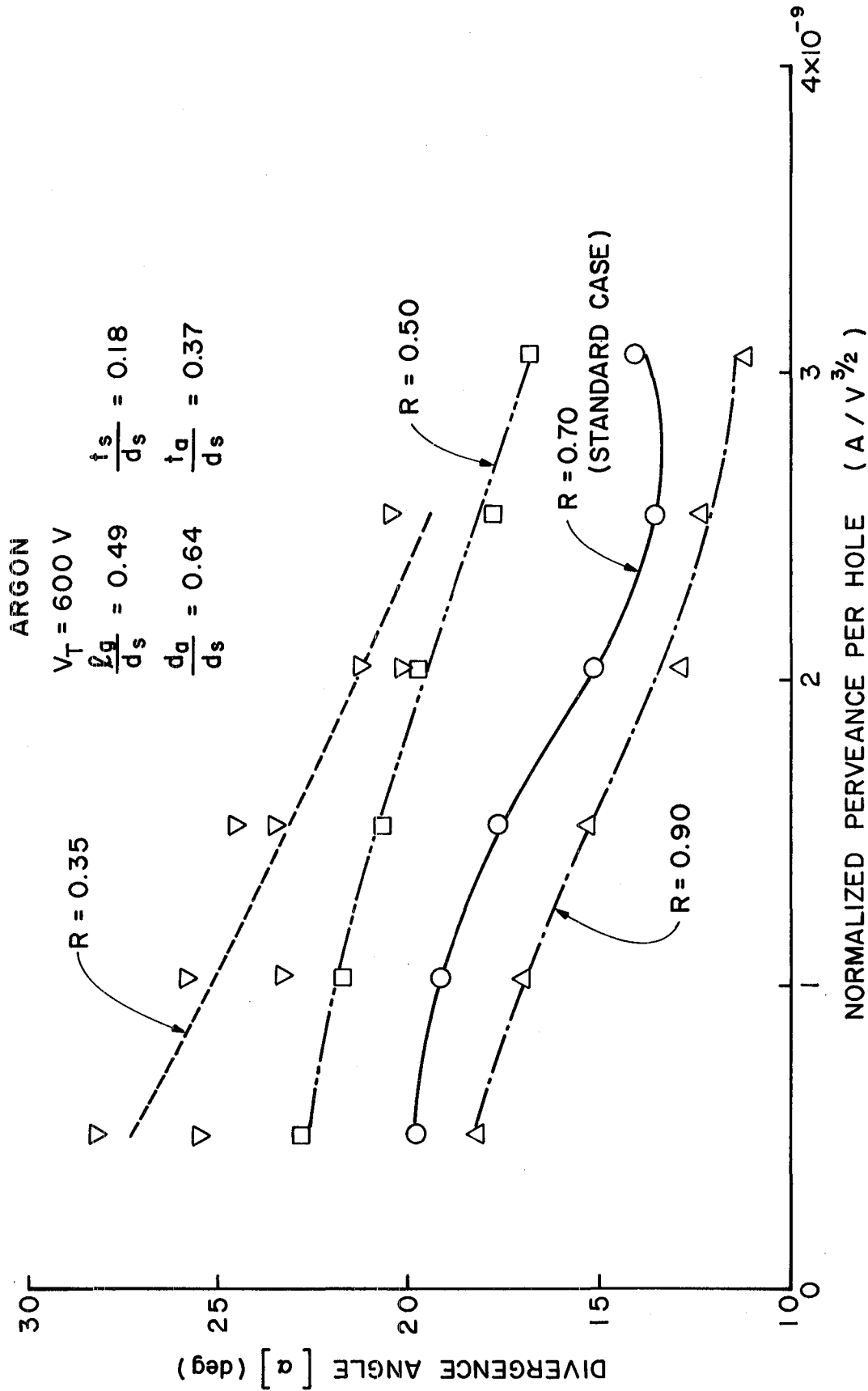
Figure 9. Effect of Net-to-Total Accelerating Voltage Ratio on Divergence

fixed grids in which the alignment could be maintained more precisely, his data are considered to give the more accurate values for divergence angle. They should therefore be used for design calculations throughout the useful range of beamlet deflections. No further data pertaining to divergence will be presented here.

Effect of Normalized Perveance Per Hole

The effect of increasing the normalized perveance (or normalized beamlet current level) at which a grid set is operating always has the effect of decreasing the usable deflection angle range. As one continues to increase the perveance an unacceptable impingement level is eventually observed even at the zero grid offset condition. If a moderate beamlet steering capability is desired, this suggests the grid-hole pair must be operating well below the maximum obtainable (aligned aperature) perveance. Figure 8 shows the shape of a typical divergence angle vs. perveance curve. One would generally want to operate at the minimum of this curve, but this corresponds to a rather high perveance condition where the beamlet cannot be deflected substantially without inducing a high impingement current (less than approximately 4° as will be seen from Fig. 10 which will be discussed in the next section). Consequently, although the divergence angle shows little change with grid offset, as suggested by Fig. 6a, the beamlets would generally have to be operating at a perveance below the one for minimum divergence in order to facilitate operation at a moderate offset without high impingement.

All of the experiments suggest that perveance has a small effect on the deflection-to-offset angle ratio (β/δ). This can be seen by

inspecting the deflection-to-offset angle plots which will be presented
(Figs. 11, 13, 14, 17, 18, 21) and noting that the curves of β/δ versus
normalized perveance are relatively flat.

Effect of Grid Separation Distance

The deflection angle range is observed in Fig. 10 to decrease as
the separation distance between the grids is increased. This can be
explained by noting that the total voltage remains constant as the
separation distance is increased and that this results in a weaker
electric field, E_1, between the grids. It can be seen from Eq. (16)
for the thin lens focal length that this will result in a larger abso-
lute value of f by noting that E_2 and E_1 are of opposite sign. A
longer focal length corresponds to a weaker lens and therefore there
is less deflection for a given grid displacement. Figure 11 shows that
the ratio of the beamlet deflection angle to the grid offset angle
(β/δ), as opposed to the ratio of the beamlet deflection angle to grid
displacement distance (β/λ), is independent of the grid separation ratio
over the full range of perveance investigated. This is not surprising
because one can combine a first order expansion of Eq. (1):

$$\delta \approx \frac{\lambda}{\ell_g + t_s} \tag{26}$$

and Eq. (20) to obtain the following expression for this deflection-to-
grid-offset ratio:

$$\frac{\beta}{\delta} \approx -\frac{(\ell_g + t_s)}{4\,\ell_g} \quad . \tag{27}$$

Equation (27) shows this ratio β/δ should indeed be independent of
the grid separation ratio to first order for this case of a thin screen
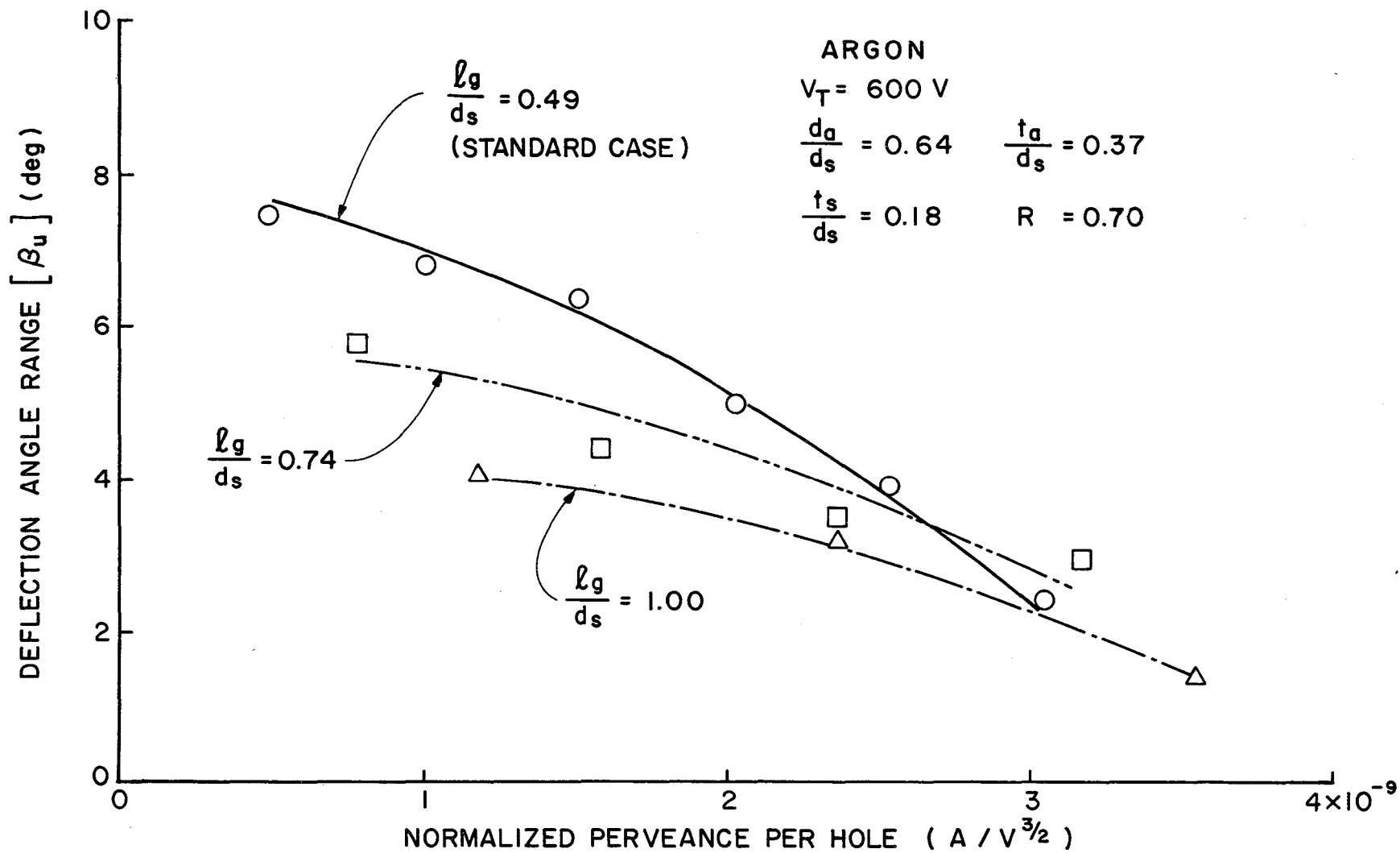
Figure 10. Effect of Grid Separation Distance on Deflection Angle Range
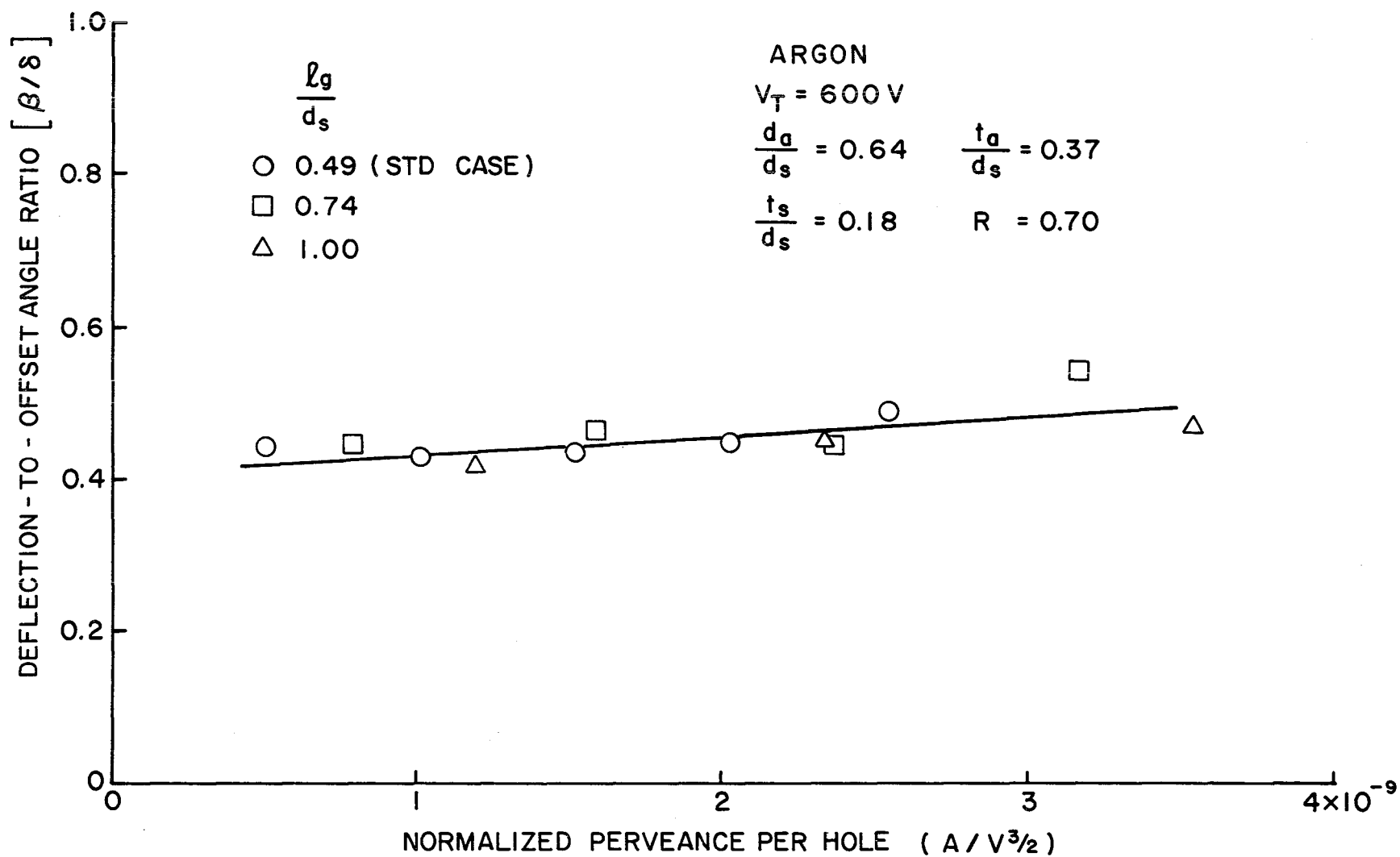
Figure 11. Effect of Grid Separation Distance on Deflection-to-Offset Angle Ratio

grid ($t_s \ll \ell_g$). The independence of the deflection angle-to-grid

offset angle ratio also confirms its preference as a correlating factor

over other factors such as the ratio of deflection angle to the linear

grid displacement (β/λ) which has been used by some other investigators.[8]

Effect of Accelerator Hole Diameter

Accelerator hole diameters larger than the standard value enable

grid sets to operate over much larger deflection angle ranges, as shown

in Fig. 12. This is presumably due to the fact that the beamlets have

more room to deflect before being intercepted by the accelerator grid.

One can also look at Fig. 12 in another way. Namely, that larger

accelerator holes will permit a given beamlet deflection at a much

higher perveance level. It is noted that power supply limitations pre-

vented operation at impingement limited perveance levels with the larger

accelerator grid hole diameters used in this study. The accelerator hole

diameter had the largest effect on the deflection angle range of all the

parameters investigated.

Figure 13 shows that the accelerator hole diameter had no signif-

icant effect on the deflection-to-offset angle ratio. Because of this

result, the observed decrease in deflection angle range with decreases

in accelerator hole diameter ratio below unity can be attributed entirely

to the onset of high accelerator grid impingement currents. The linear

optics theory presented in Section II did not consider variations in

the accelerator hole diameter ratio. It is considered a particularly

significant experimental result that changes in the relative sizes of

the apertures did not affect the ratio of beamlet deflection to grid

aperture displacement.
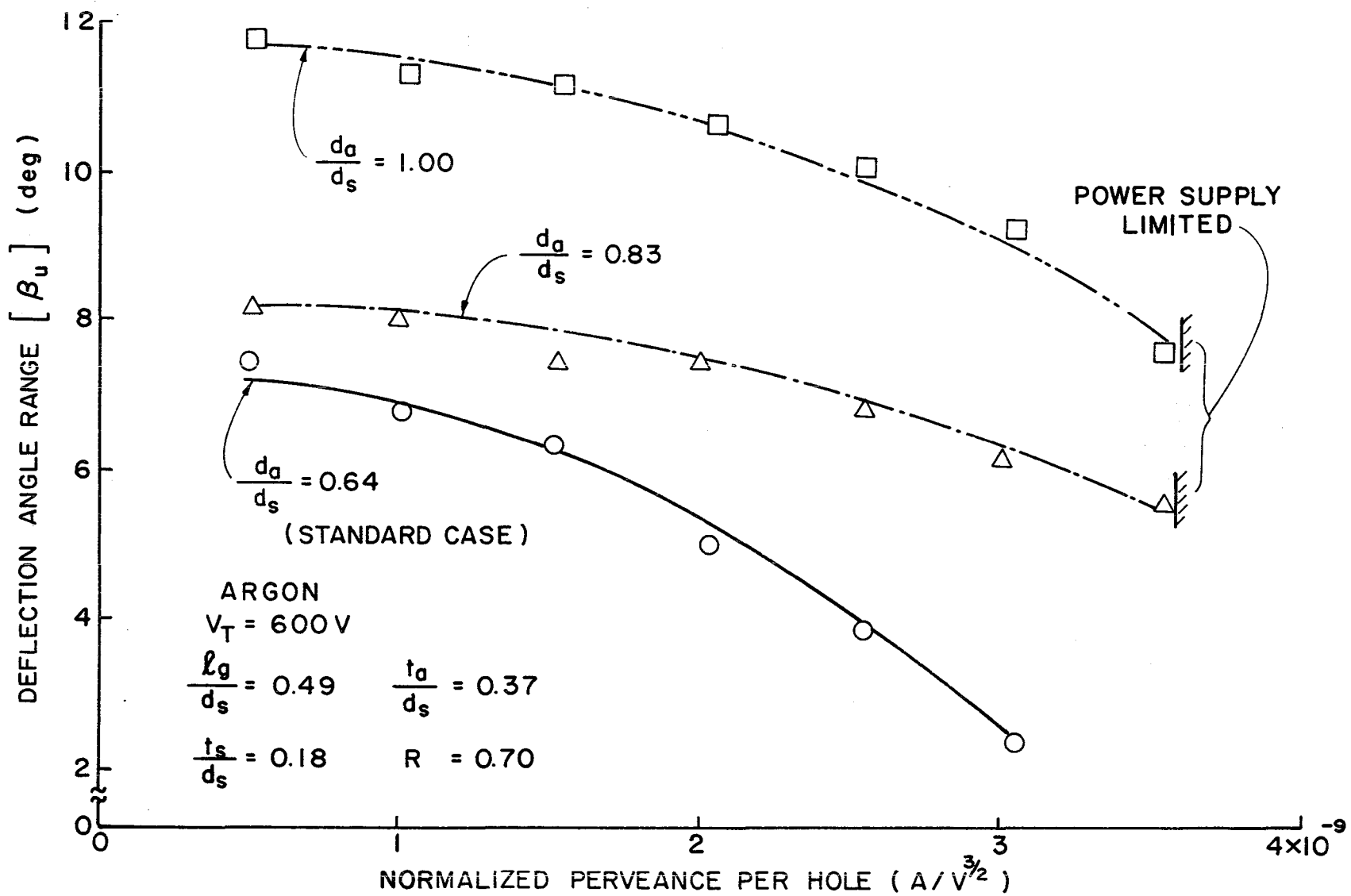
Figure 12. Effect of Accelerator Grid Hole Diameter on Deflection Angle Range
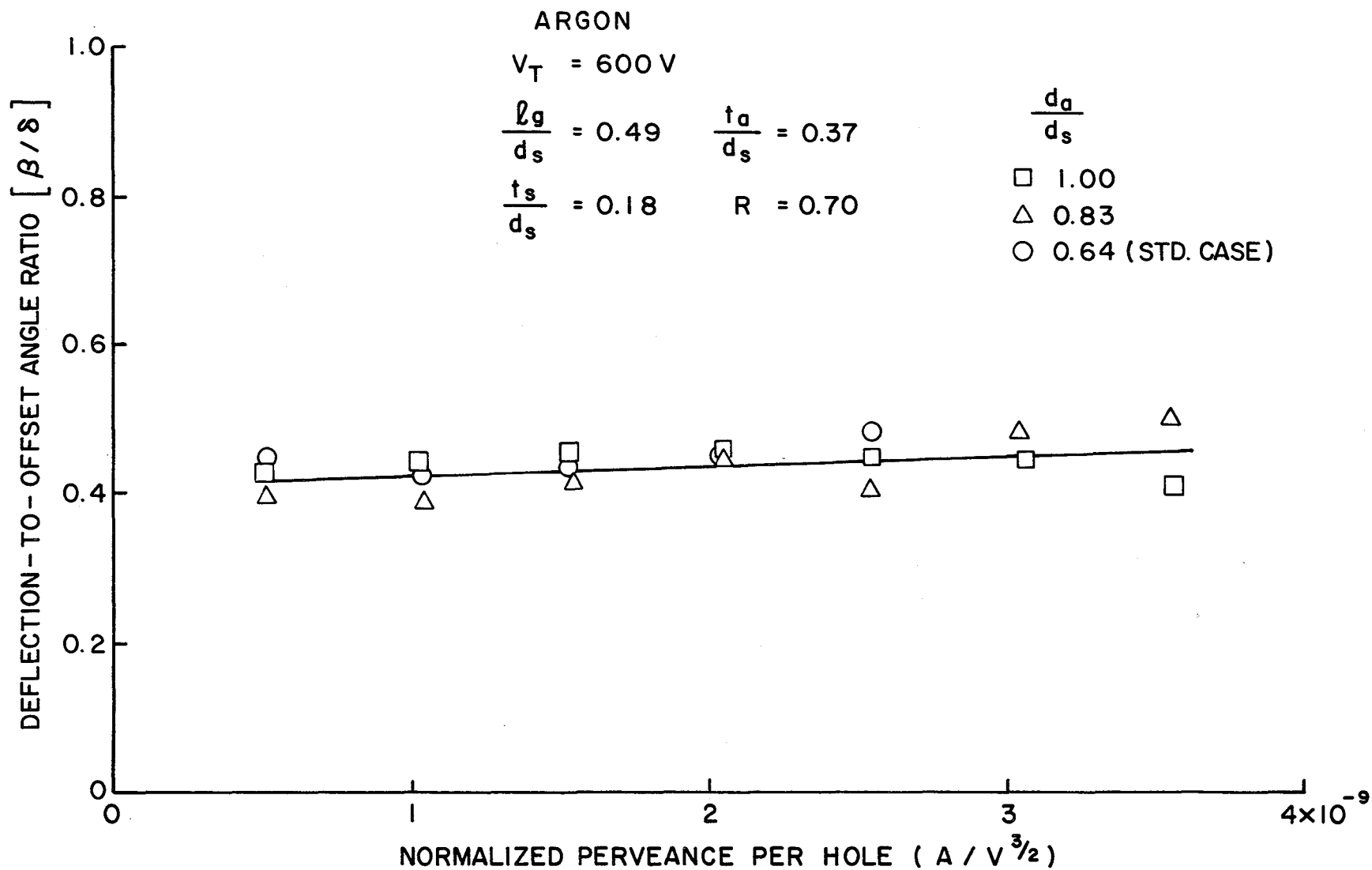
Figure 13. Effect of Accelerator Grid Hole Diameter on Deflection-to-Offset Angle Ratio

Effect of Net-to-Total Accelerating Voltage Ratio

The net-to-total voltage ratio (R) has a moderate effect on the deflection-to-offset angle ratio (β/δ). As the R-value decreased from 0.90 to 0.35, β/δ increased from 0.4 to 0.6, as shown in Fig. 14. This is explained by recognizing that at a constant total voltage, a decrease in the R-value is accompanied by an increase in the absolute value of the downstream deceleration field (E_2). The ions therefore undergo a greater total deflection as they are subjected to this additional elec- tric field, which has been distorted by the asymmetrical geometry of the displaced grids. This effect is incorporated in the linear optics theory by the ($1-E_2/E_1$) term of Eq. (19).

One might expect that an increase in β/δ for lower R-values would be accompanied by larger deflection angle ranges. Figure 15, however, shows that the deflection angle range has only a slight dependence on the R-value as long as R is greater than about 0.5. It is quite likely that the beamlet diameter at the plane of the accelerator grid increases for lower R-values and therefore more nearly fills the accelerator grid aperture. The impingement limit is therefore reached at similar deflec- tion angle ranges for all of these R-values. When the R-value is re- duced to about 0.35, however, the impingement limit becomes much more severe and this results in a more restricted deflection angle range occurring at the higher perveance levels.

Effect of Total Acceleration Voltage

An inspection of Eq. (19), which pertains to linear optics theory, reveals that the total acceleration voltage (V_T) does not appear di- rectly, so it would not be expected to affect the beamlet deflection

Figure 14.   Effect of Net-to-Total Accelerating Voltage Ratio on Deflection-to-Offset Angle Ratio
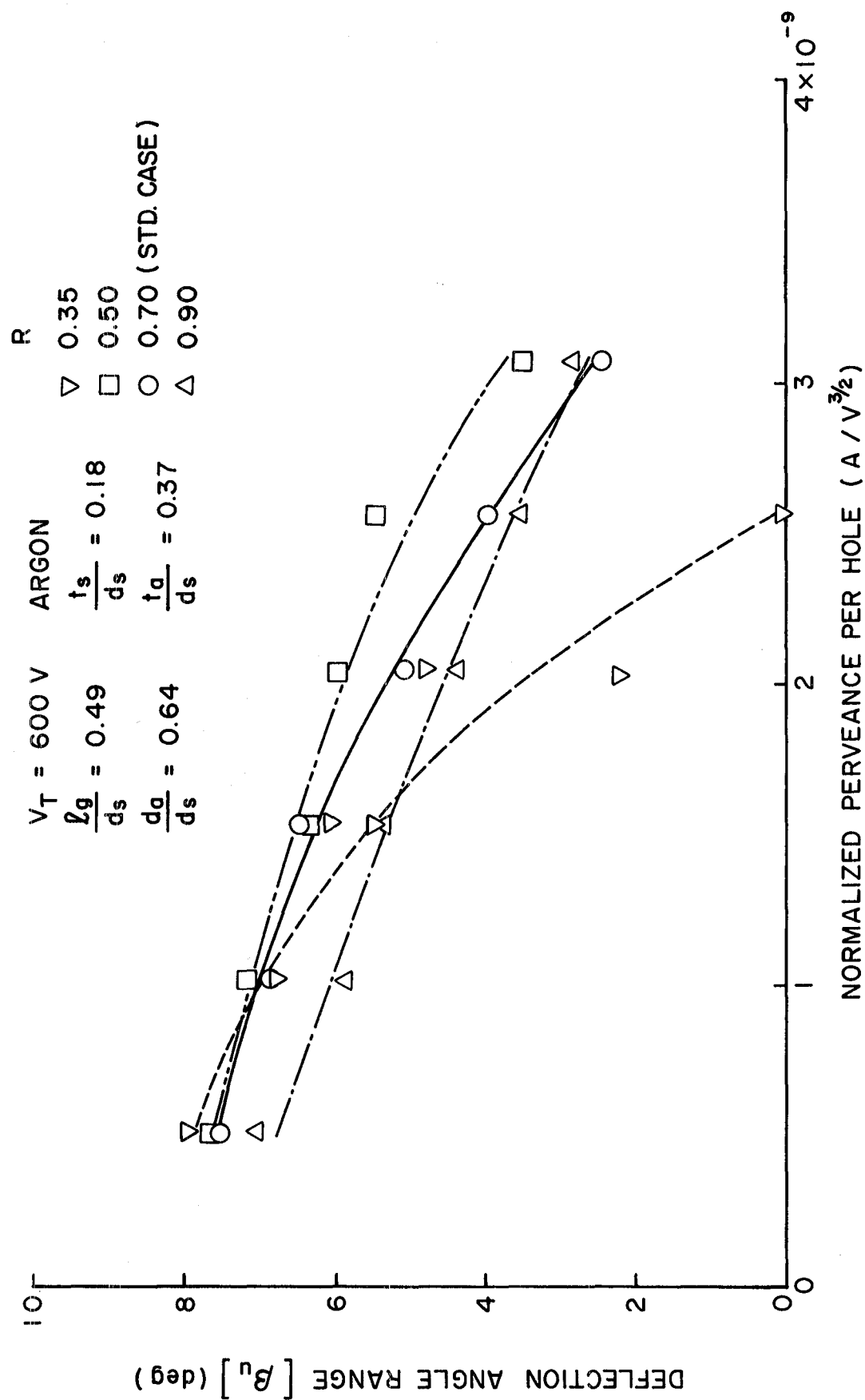
Figure 15. Effect of Net-to-Total Accelerating Voltage Ratio on Deflection Angle Range

to first order. The effect of total accelerating voltage is incorpora-
ted into Eq. (19) approximately through the potential field E_1, but
the factor $(1-E_2/E_1)$ from Eq. (19) is constant for a given R-value re-
gardless of the value of V_T. Figure 16 does show however that the de-
flection angle range increases slightly when the total accelerating
voltage is nearly doubled from 600 v to 1100 v. Figure 17 shows that
while the magnitudes of the deflection-to-offset angle ratio are com-
parable at the two voltages, changes in perveance seem to induce a
greater change in this ratio at the higher voltage.

It should be noted that some of the data on Figs. 16 and 17 in-
volved operation of the ion source at a slightly higher discharge volt-
age and magnet current. This did not appear to alter the data trends.
It was done so the ion source discharge could be sustained at the
higher beam currents associated with perveance limited operation at the
1100 v condition.

Effect of Accelerator Grid Thickness

As shown in Fig. 18, the accelerator grid thickness had no signifi-
cant effect on the deflection-to-offset angle ratio. However, in Fig. 19
the thickest accelerator grid is seen to exhibit a pronounced reduction
in deflection angle range. This is considered to be due to the fact
that interception of the beamlet on the downstream edge of the accel-
erator grid occurs at a much smaller grid displacement with the thickest
grid. It is noteworthy that a very thin accelerator grid showed no
improvement in the deflection angle range over that observed for the
standard case thickness, presumably because there is a threshold thick-
ness effect. These data suggest that there is no particular advantage,
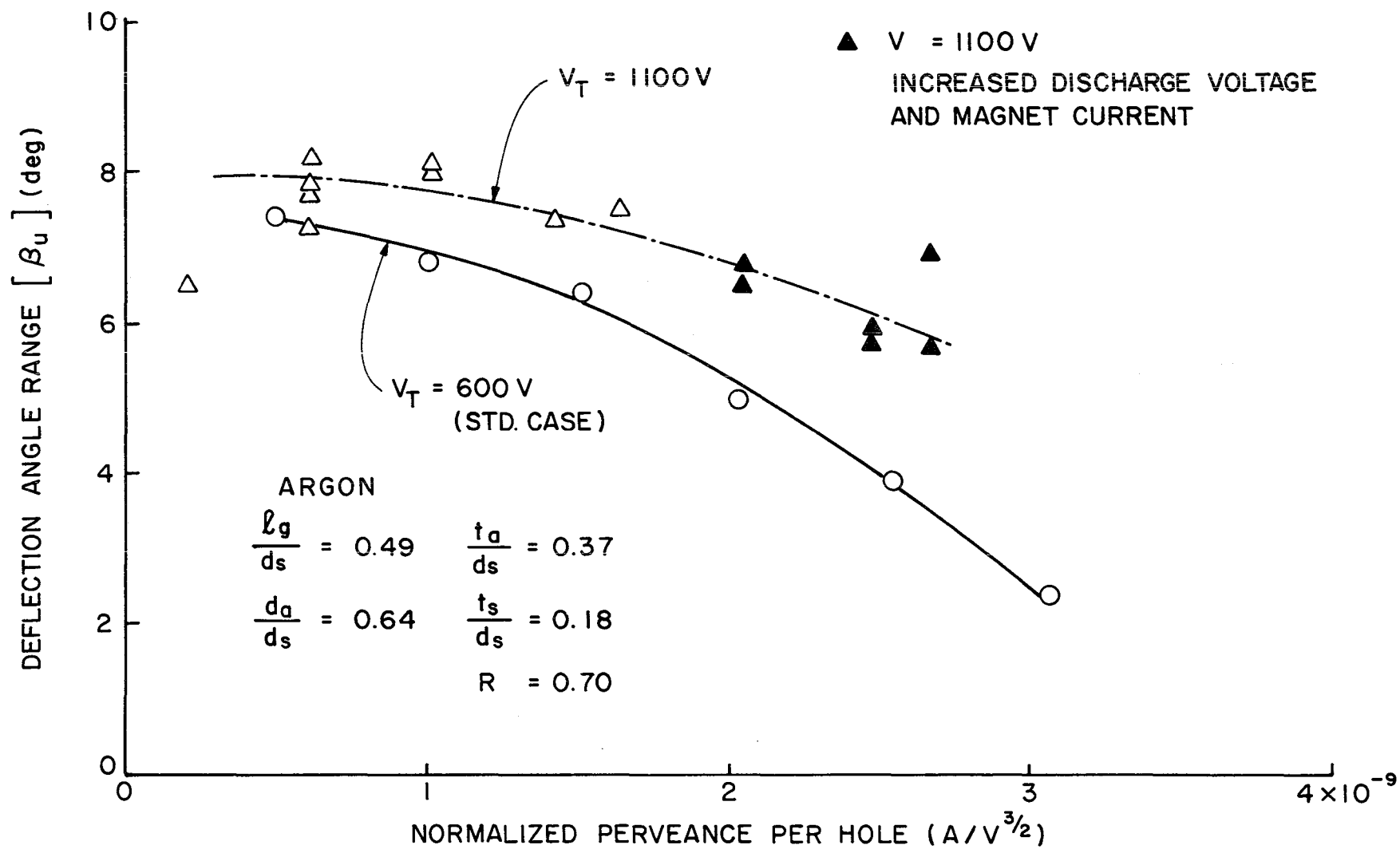
Figure 16. Effect of Total Accelerating Voltage on Deflection Angle Range

ARGON

$\dfrac{\ell_g}{d_s} = 0.49 \qquad \dfrac{t_a}{d_s} = 0.37$

$\dfrac{d_a}{d_s} = 0.46 \qquad \dfrac{t_s}{d_s} = 0.18$

$R = 0.70$

$V_T = 1100\,V$

$V_T = 600\,V$
(STD. CASE)

▲ $V_T = 1100\,V$

INCREASED DISCHARGE
VOLTAGE AND MAGNET
CURRENT

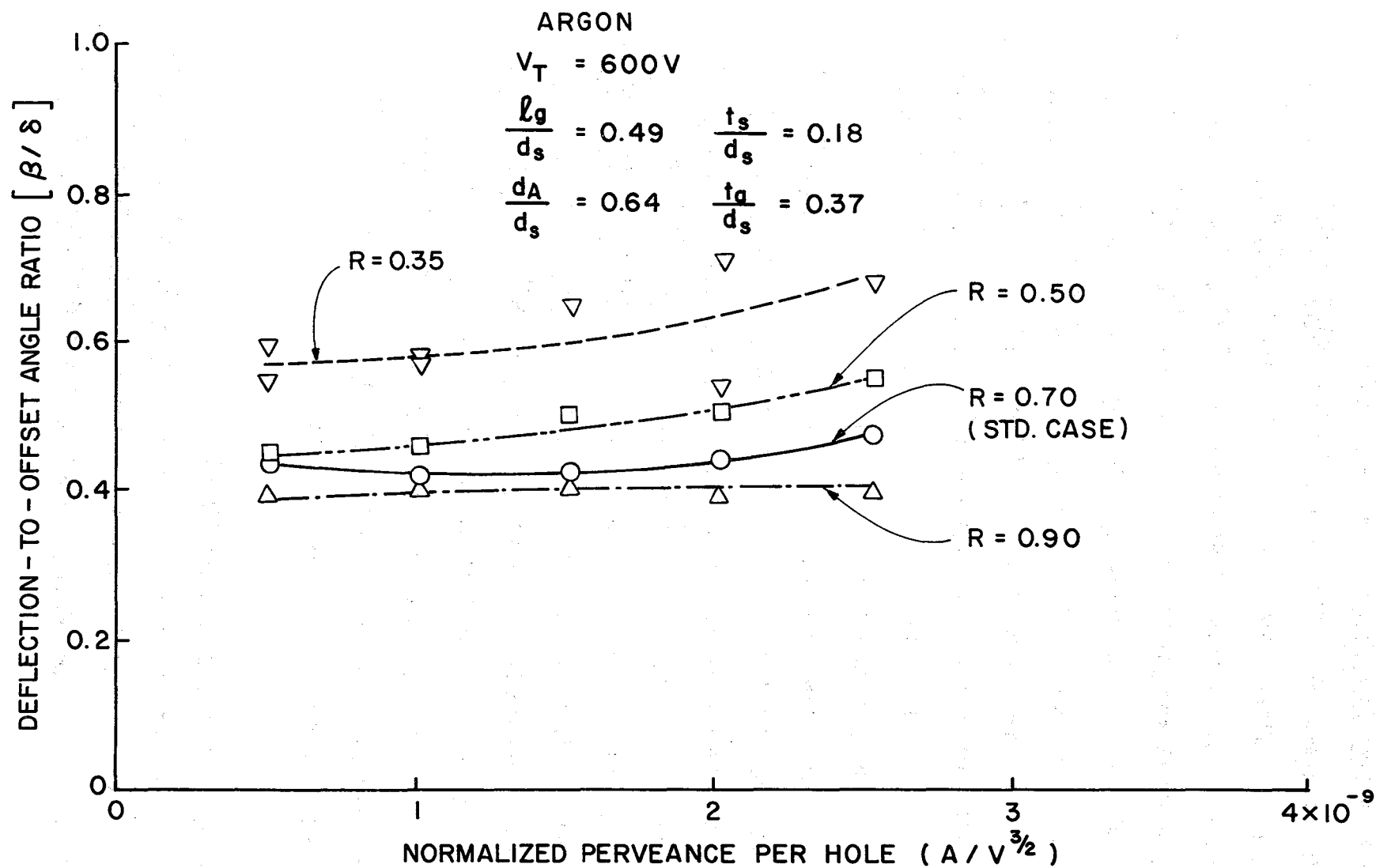DEFLECTION-TO-OFFSET ANGLE RATIO $[\beta/\delta]$

NORMALIZED PERVEANCE PER HOLE $(A/V^{3/2})$
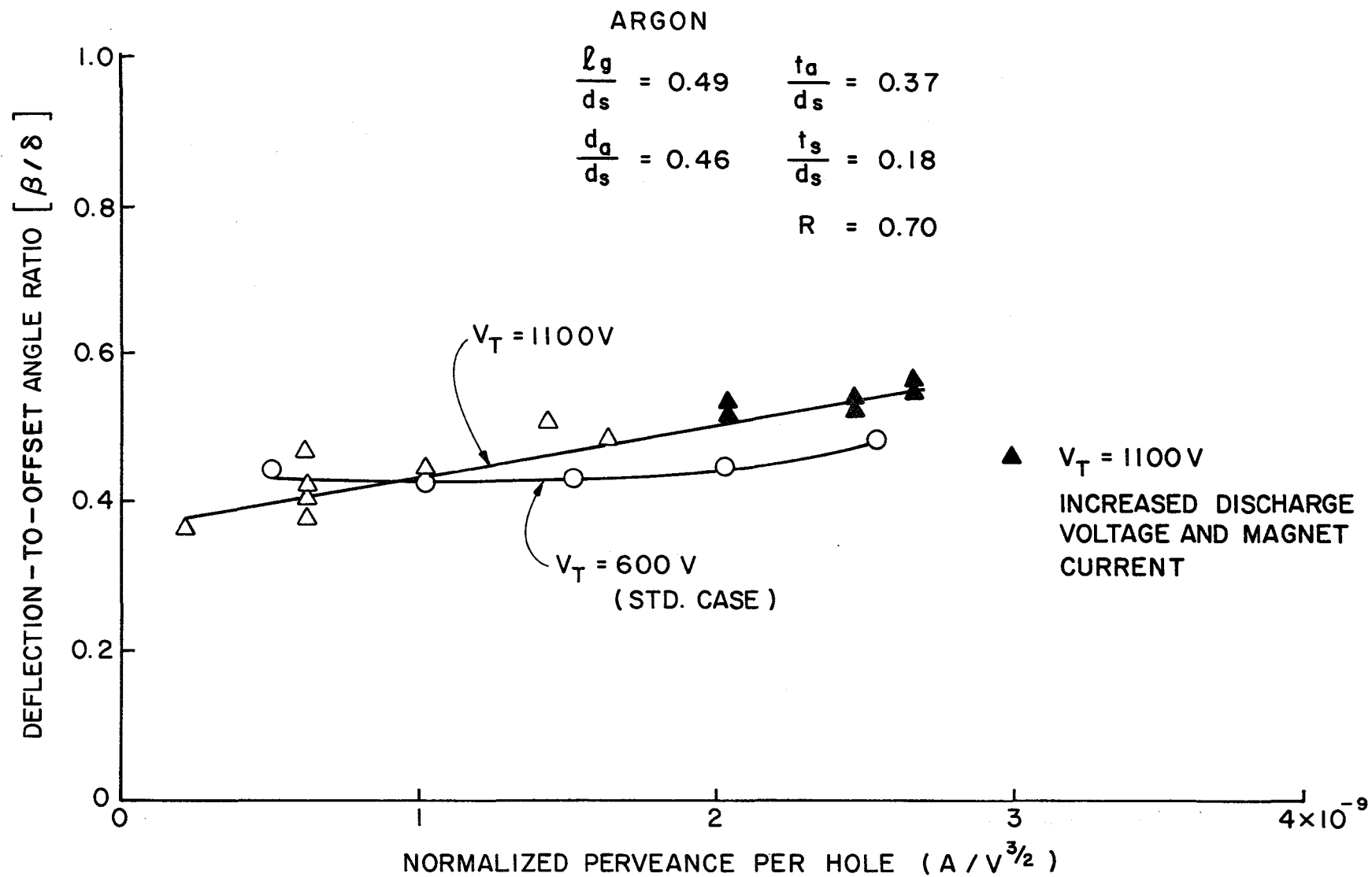
Figure 17. Effect of Total Accelerating Voltage on Deflection-to-Offset Angle Ratio
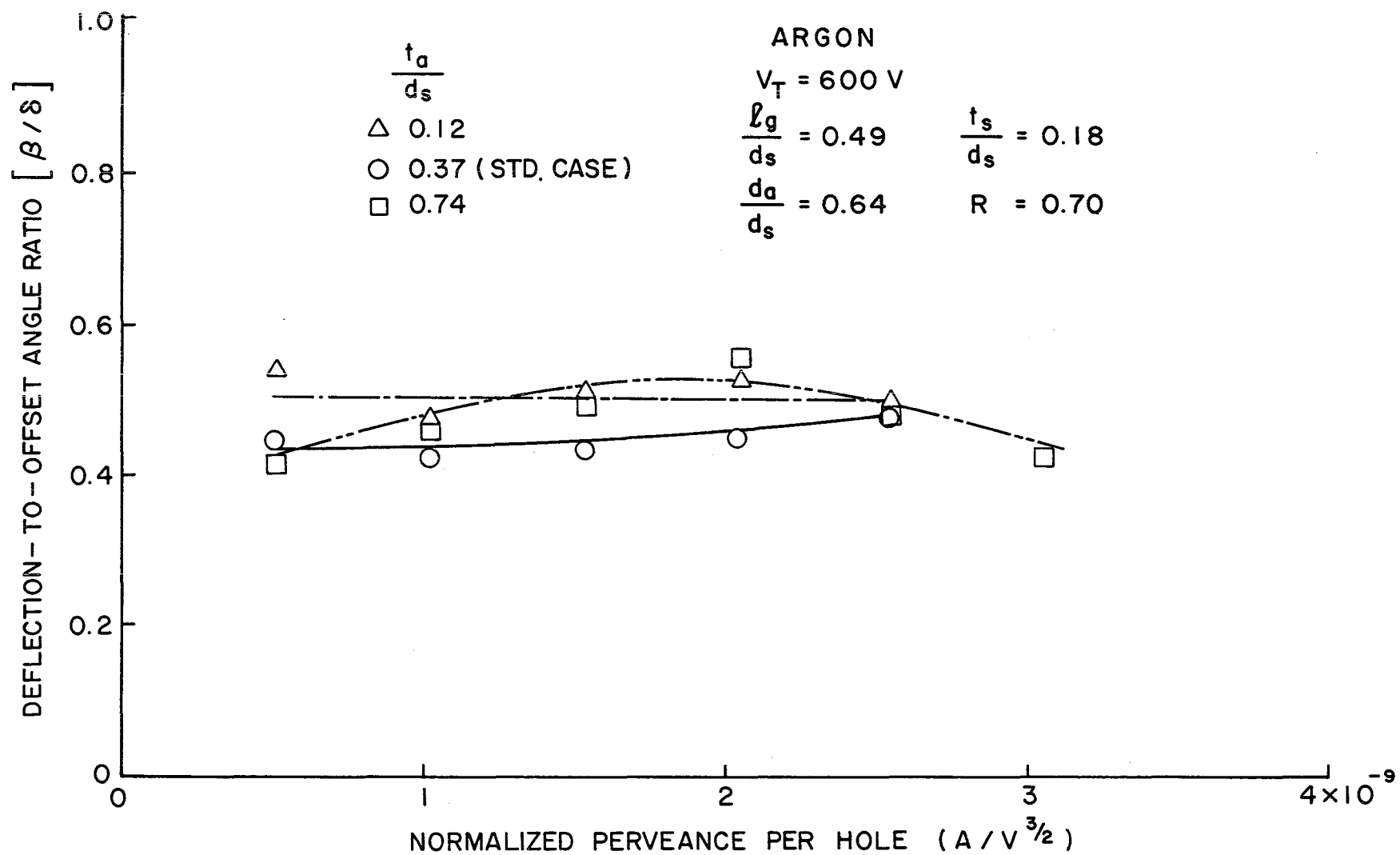
Figure 18. Effect of Accelerator Grid Thickness on Deflection-to-Offset Angle Ratio

43
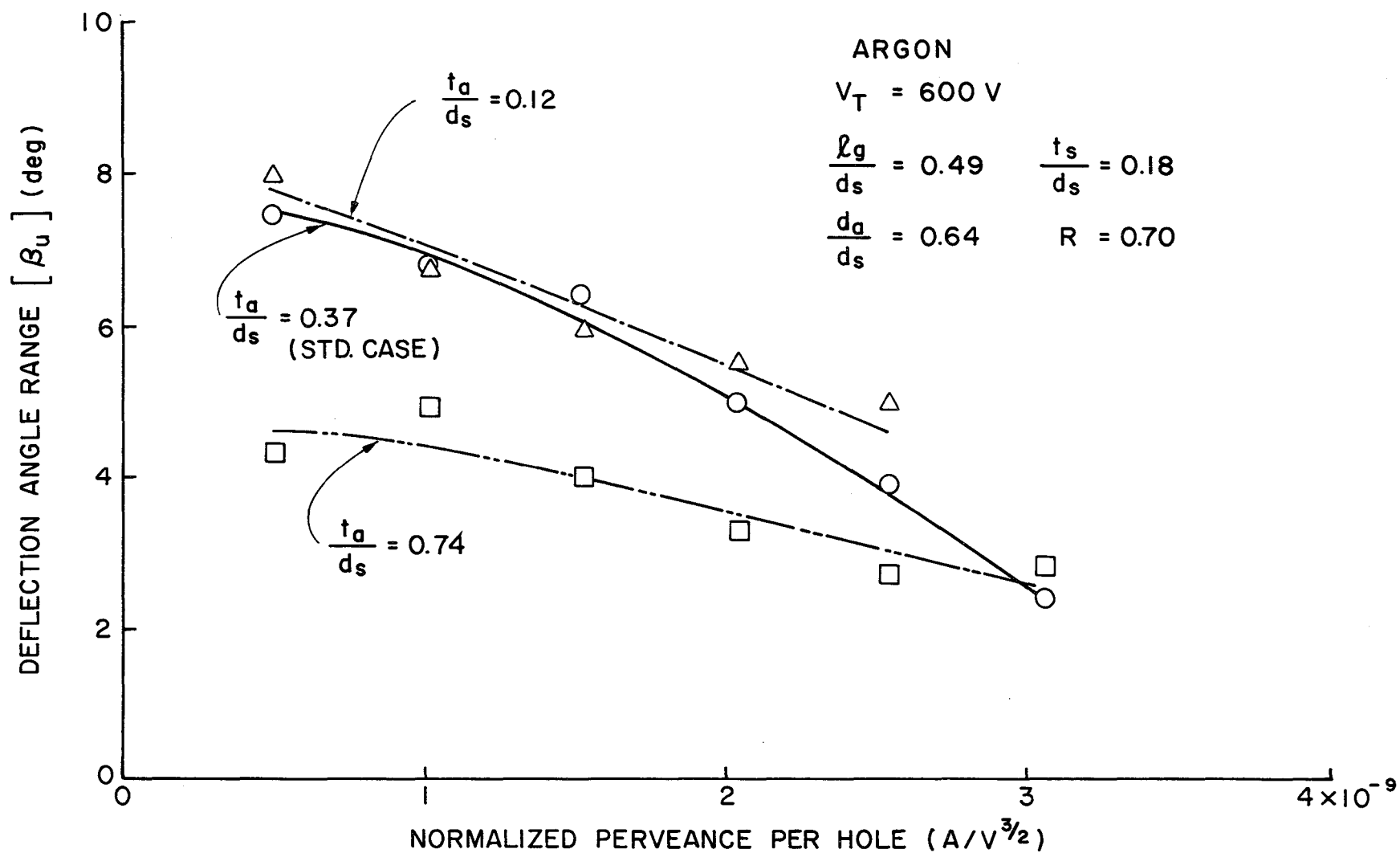
Figure 19. Effect of Accelerator Grid Thickness on Deflection Angle Range

from a beamlet deflection standpoint, in using extremely thin accelerator grids and incurring the higher neutral propellant atom loss rate associated with the thinner accelerator grids.

Effect of Screen Grid Thickness

The effect of doubling the standard screen grid thickness on the deflection characteristics of beamlets is examined in Figs. 20 and 21. This change has a small effect on the beamlet deflection characteristics. A slight reduction in deflection range is observed for the thicker screen grid as illustrated in Fig. 20. This is supported by previous work by Aston[3,10] which shows that thinner screen grid geometries are capable of achieving slightly higher perveances. This is consistent with the fact that the thinner screen grid exhibits a slightly higher deflection angle range at a given perveance level. There appears to be a slight difference in the deflection-to-offset ratio for different screen grid thicknesses as shown in Fig. 21. The increase in the deflection-to-offset angle ratio for thicker screen grids observed in Fig. 21 is consistent with Eq. (27) which indicates the thickness should have a significant effect on the offset angle value when the screen grid thickness (t_s) becomes a significant fraction of the grid separation distance (ℓ_g).
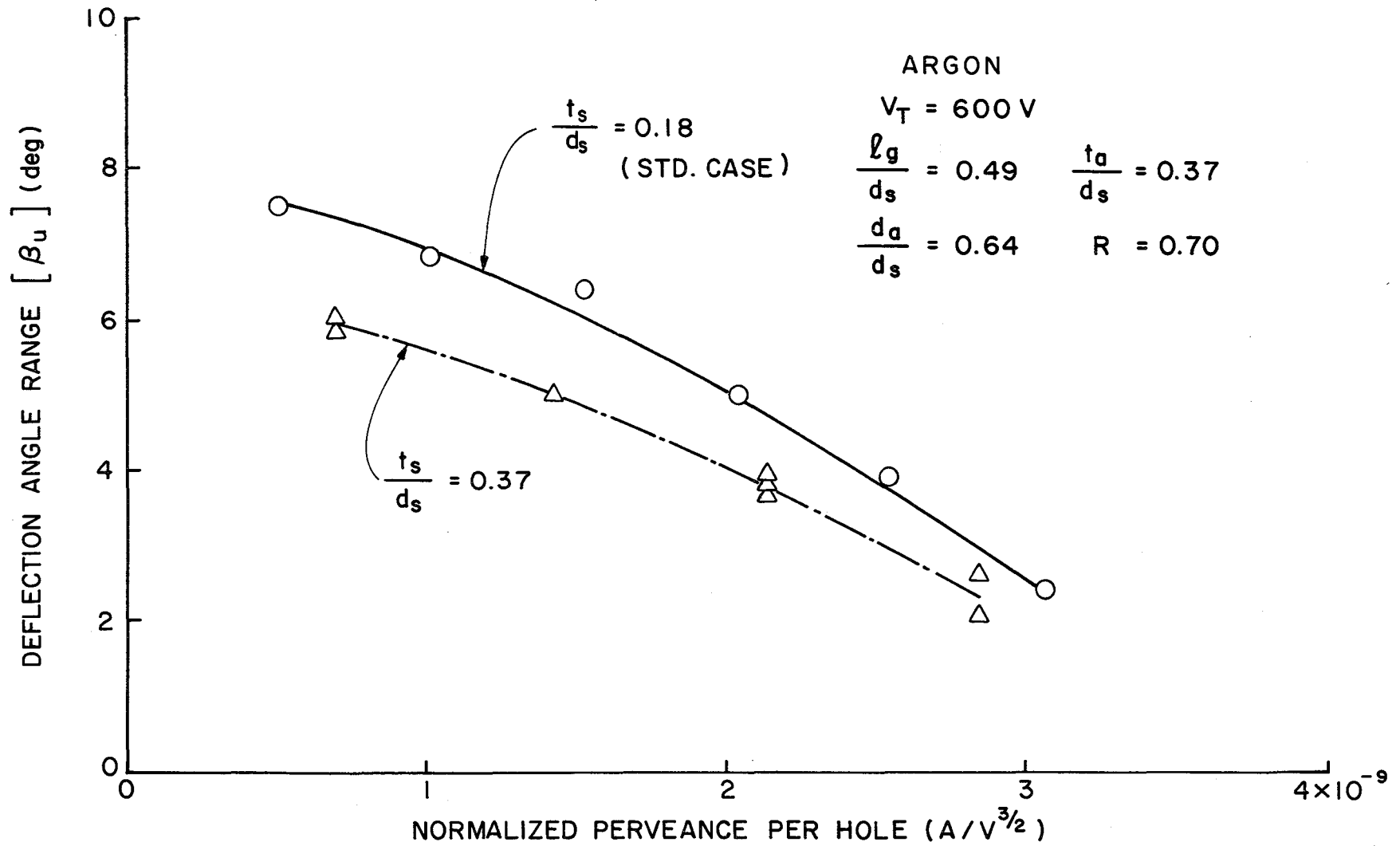
Figure 20.   Effect of Screen Grid Thickness on Deflection Angle Range

ARGON

$V_T = 600 \, V$

$\dfrac{\ell_g}{d_s} = 0.49$ $\dfrac{t_a}{d_s} = 0.37$

$\dfrac{d_a}{d_s} = 0.64$ $R = 0.70$

$\dfrac{t_s}{d_s} = 0.37$

$\dfrac{t_s}{d_s} = 0.18 \, (STD. \, CASE)$

DEFLECTION - TO - OFFSET ANGLE RATIO $[\beta / \delta]$

NORMALIZED PERVEANCE PER HOLE $(A / V^{3/2})$

47
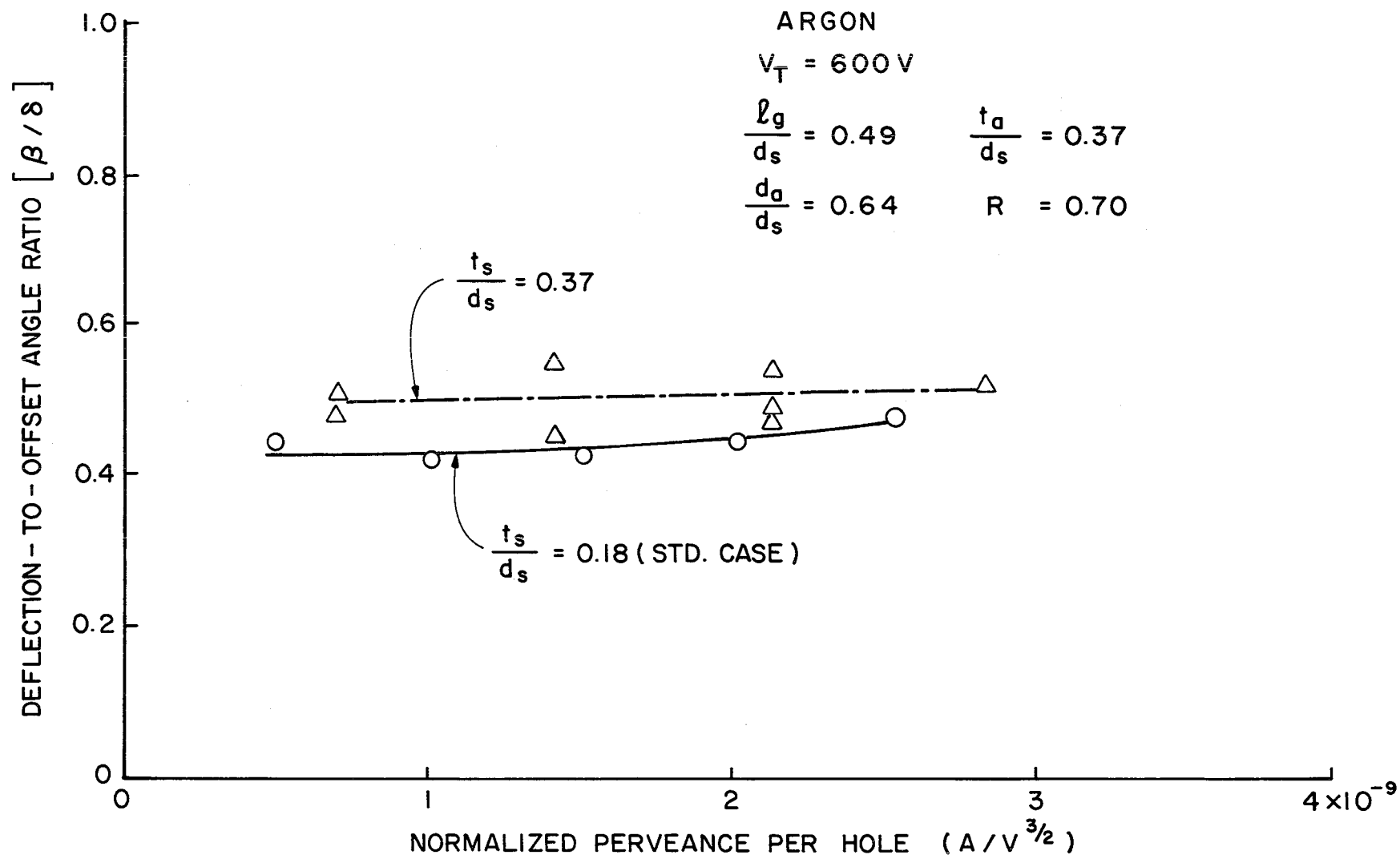
Figure 21.   Effect of Screen Grid Thickness on Deflection-to-Offset Angle Ratio

V. DISHED-GRID BEAMLET ANALYSIS

In this section the beamlet vectoring data presented in the pre-
vious section of this report will be used to examine the beamlet
deflections that would be expected in a typical dished-grid set. The
objective is to determine the effects of such design factors as dish
depth and grid hole offsets on the impingement characteristics of a
dished-grid set. In order to conduct this analysis the current density
profile and thermal distortion characteristics of a typical dished-grid
system will be examined.

The parameters used to define the particular spherically dished
grid set considered here are shown in Fig. 22. The beamlet pattern
shown suggests aligned screen and accel grid holes that would cause the
beamlets to emerge in a divergent pattern. Using current density pro-
file data for a typical ion source together with reasonable values for
grid geometric parameters, the radial screen/accel grid hole displace-
ment profile needed to correct this condition will be determined. At
this operating condition all of the beamlets would be aligned with the
thruster axis. In addition, the impingement limited perveance will be
calculated as a function of grid radius using the deflection angle range
data presented earlier in this report. This will be compared to the
actual perveance in an operating thruster to determine where high
impingement might be expected over the surface of the grids for this
thruster.
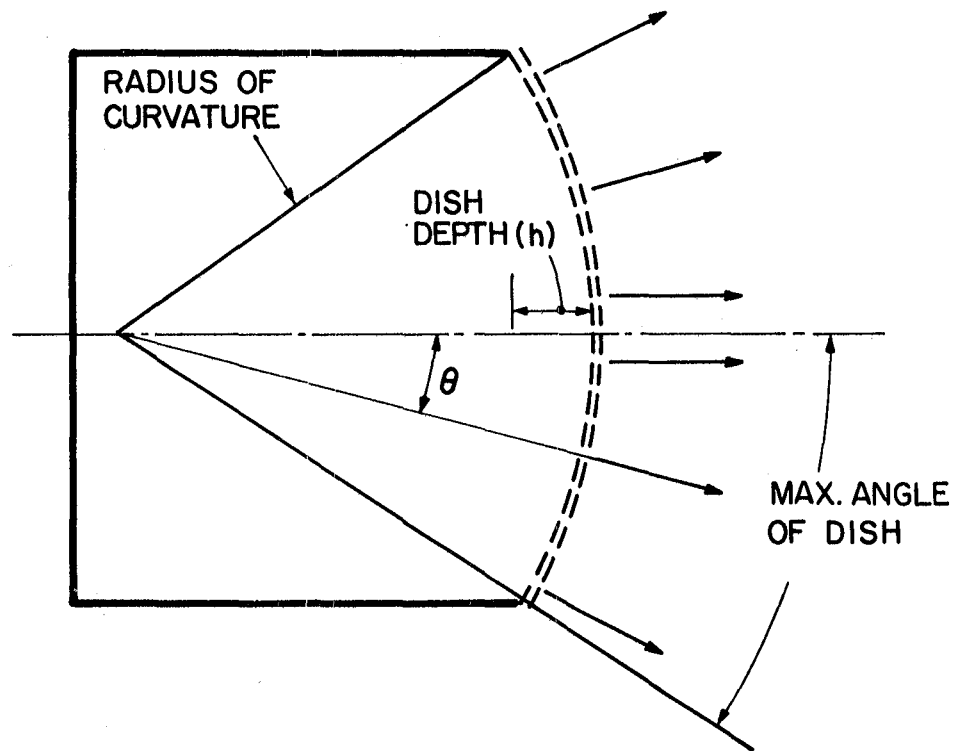
Figure 22. Dished Grid Geometry

The thruster selected for this analysis is the 30 cm dia. 800 series Engineering Model Thruster. The current per hole data, required as input for analysis of the grids, are shown in Fig. 23.[11] These data were obtained using mercury propellant when the thruster was operating at a 2.0A beam current. The current per hole values cited in Fig. 23 had to be multiplied by the square root of the mercury to argon atomic mass ratio to obtain the allowable perveance data needed for direct comparison with the data presented herein which were collected using argon propellant.

In order to determine the grid separation distance and relative hole positions at operating temperature as a function of radius, the linear, thermal expansion model of Rawlin, Banks, and Byers[12,13] was applied to the molybdenum grids and support rings of the thruster. This model assumes a constant operating temperature for each grid and grid support ring. Using a value of 5.5×10^{-6} per °C for the linear coefficient of expansion of molybdenum, the radial and axial distortion of each grid is determined with respect to the thruster centerline. This model may not be applicable to all grid assemblies, but it is useful here to illustrate the application of beamlet vectoring data to the analysis of dished-grid accelerator systems.

When a pair of grids is dished and then separated by a prescribed distance, the screen-accelerator hole pairs become mis-aligned, and the beamlets are directed severely off-axis. This requires hole-pattern compensation, which for grids dished convex downstream, implies an accelerator grid hole pattern with center-to-center hole spacings increased or a screen grid with hole spacings reduced from their initial values. By using some compensation a grid-hole pair can be re-aligned
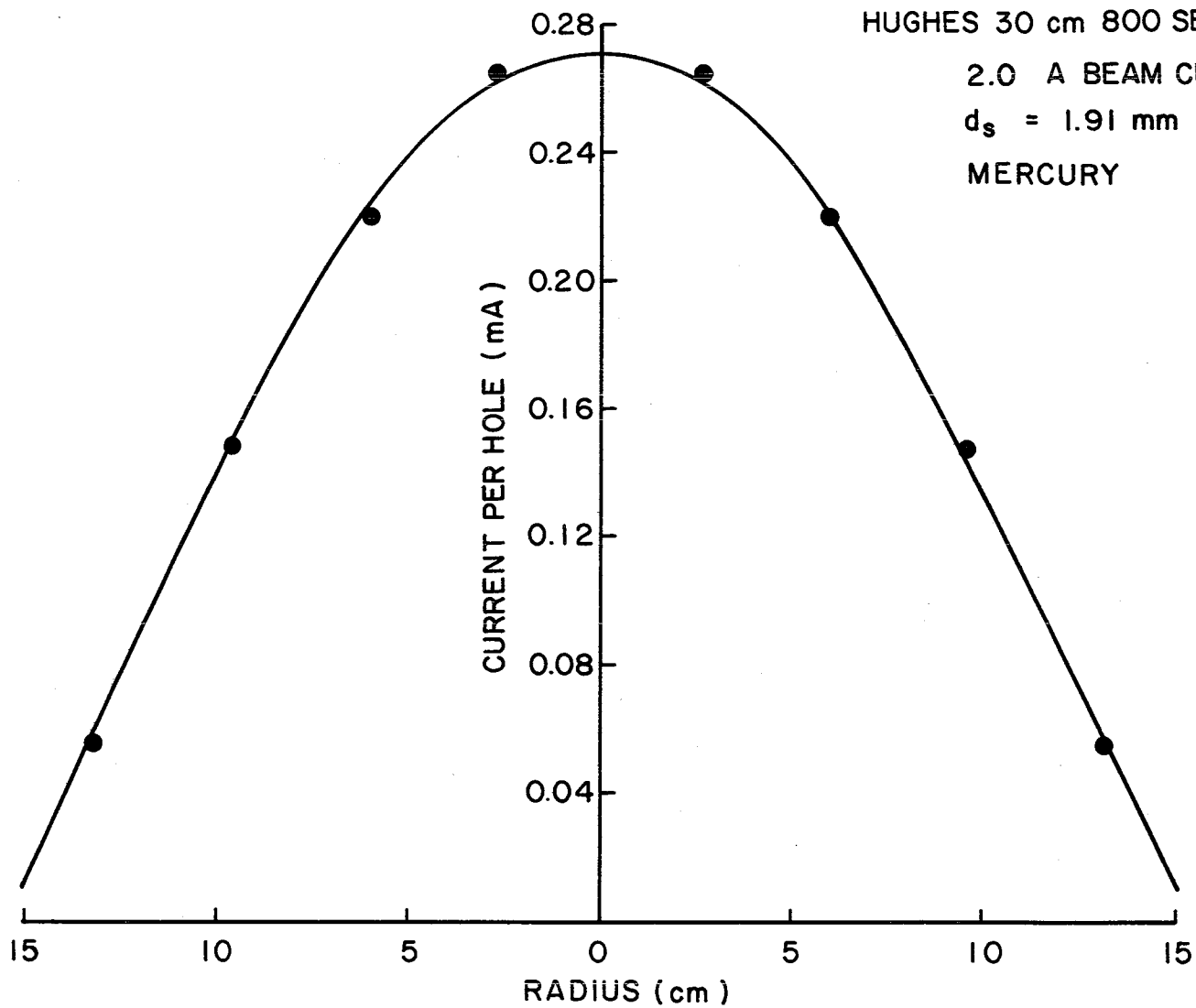
Figure 23. Current per Hole Profile for Sample 30 cm Thruster

to the zero offset angle condition, however, an additional amount will be required in order to cause each beamlet to be directed away from the grids along lines parallel to the thruster axis (para-axial lines). In order to correct for these two effects, the accelerator grid hole spacings over the entire grid surface are increased by a constant factor which is $(1 + \kappa)$ times the screen hole spacings, where κ is the accelerator grid compensation fraction. Once a particular value of κ is chosen, the grid thermal effects can be applied to a given grid geometry. Figure 24 shows the effects of various accelerator compensations on the screen-accelerator grid-hole alignment as a function of radius for a given dished-grid set. The thermal distortions predicted from the grid thermal model[12,13] have been used to determine changes in grid separation and relative grid axis displacements. These in turn have been used to compute the grid offset angles appropriate to each radial location. Also shown in Fig. 24 as a solid line is the offset angle required as a function of radius to produce para-axial beamlets. It is determined from a deflection-to-offset plot of data presented in Section IV (Fig. 13 for this case where $R = 0.70$ and $d_a = d_s$) using as the required deflection angle (β), the angular separation between the thruster centerline and the normal to the accelerator grid surface at each radial location in the 30 cm dished-grid thruster (θ in Fig. 22).

Figure 25 presents the same type of data as Fig. 24 but in this case the dish depth is one half the previous value. The magnitude of the dish depth affects the value of grid offset angle needed to induce re-alignment of all of the beamlets with the thruster centerline. A comparison of Figs. 24 and 25 shows that the smaller dish depth requires much less grid offset for the outer radius holes, and therefore it would

Figure 24. Dished Grid Offset Angles at Operating Temperatures for Various Accelerator Grid Compensations, Cold Dish Depth 2.25 cm, Cold Grid Separation Distance 0.94 mm
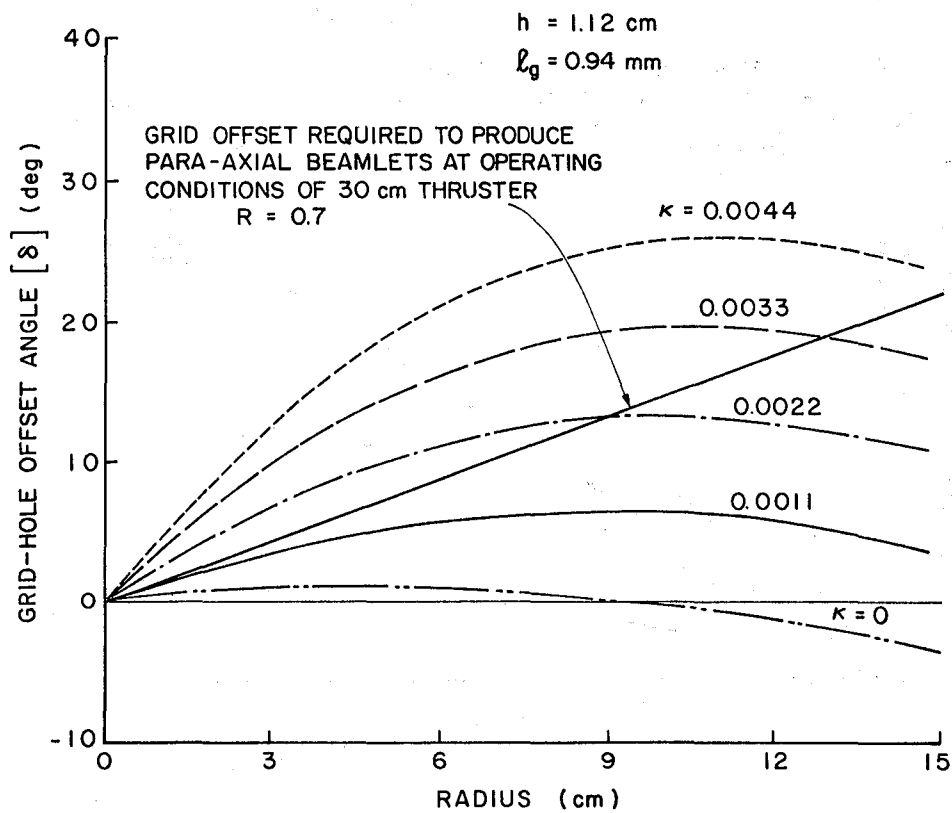
Figure 25. Dished Grid Offset Angles at Operating Temperatures for
Various Accelerator Grid Compensations, Cold Dish Depth
1.12 cm, Cold Grid Separation Distance 0.94 mm

be expected that the outer holes could then be operated at higher per-veance levels.

The drawback to using a smaller dish depth is that this leads to greater changes in the screen grid-to-accelerator grid separation distance when the cold grid is brought to operating temperature. Figure 26[12] shows the change in separation distance between the grids as a function of the thruster radius for several values of dish depth. The figure shows that the largest amount of thermal distortion occurs for the smallest dish depth. This effect could be corrected for one operating temperature by varying the initial grid separation distance as a function of thruster radius, perhaps by using different dish depths for the screen grid and accelerator grid. It is also apparent from Figs. 24 and 25 that a single value of accelerator grid compensation (κ) does not produce the required grid offset over the entire grid surface for the thermal deformations assumed here. Since grids are commonly fabricated by photo-etching a hole pattern onto the grid material, a hole pattern could be generated which incorporates the correct compensation for each radial location. Another approach would be to note in Fig. 24 that a single value of compensation is a good approximation to the line for para-axial beamlets over one-half to two-thirds of the thruster radius in this case. Using this value of compensation over the entire grid surface results in the outer radius beamlets not being steered through an angle large enough to make them emerge parallel to the thruster axis. However, this loss in thrust density may be an acceptable alternative to a more complicated grid design.

For a given dish depth the grid separation distance selected also influences the amount of accelerator grid compensation needed for
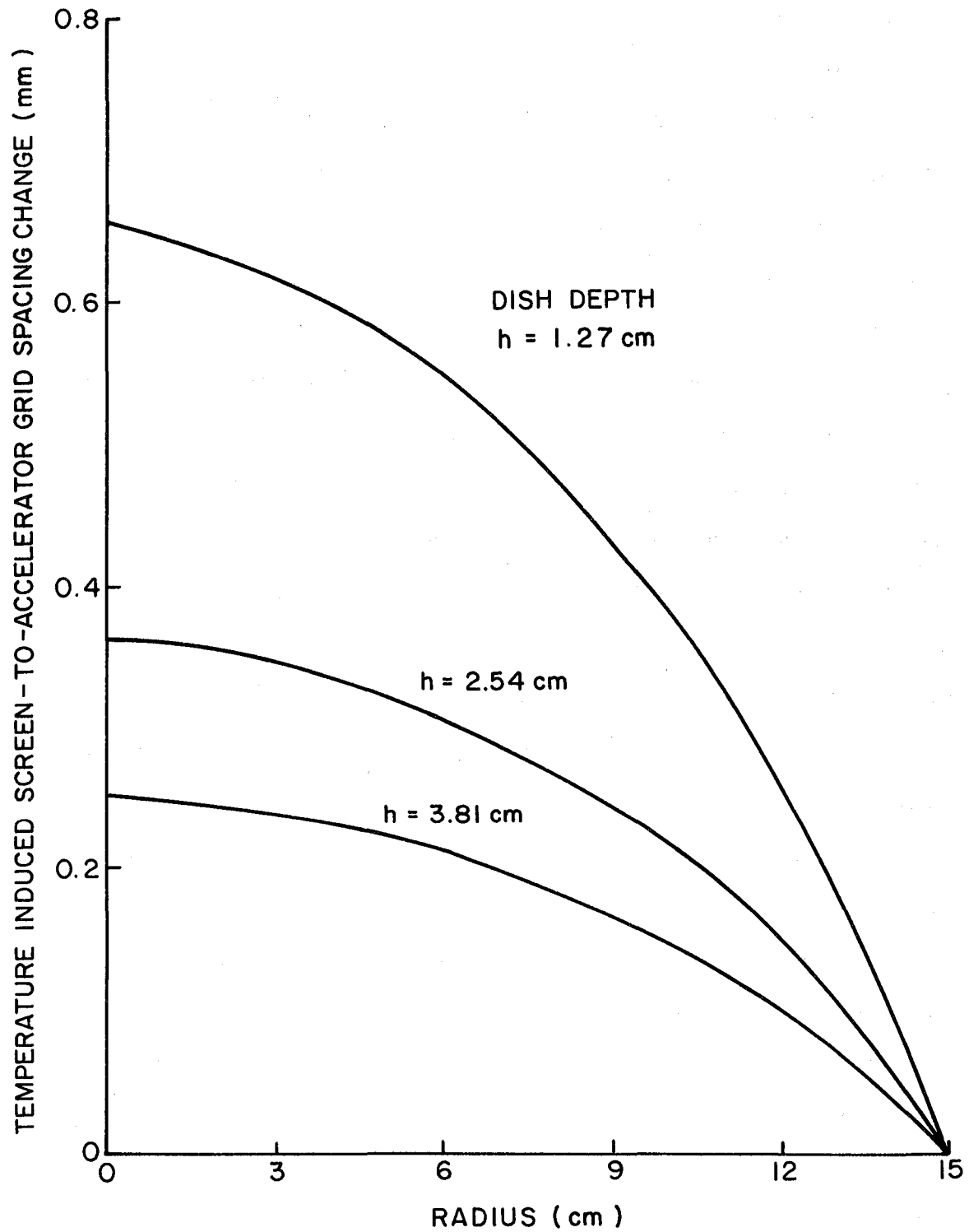
Figure 26. Effect of Dish Depth on Temperature Induced Grid Spacing
Change

beamlet alignment. A comparison of Fig. 27 with Fig. 24, both calcu-
lated with the same dish depth, but using different initial gap dis-
tances shows that the case with the smaller gap distance requires less
accelerator grid compensation. This is caused by two effects that can be
understood by considering the case where a screen-accelerator grid hole
pair from a dished-grid set are initially aligned for a grid separation
distance equal to zero. As the separation distance is increased the
accelerator grid hole axis becomes increasingly displaced with respect
to the screen hole axis, therefore the smaller gap distance results in
a smaller initial hole displacement. Also, for a screen-accelerator
hole displacement produced by a given compensation fraction, Eq. (1)
shows that a smaller grid separation distance results in a larger off-
set angle and hence a greater beamlet deflection.

Information such as that which is presented in Figs. 24-27 for the
present case can be used to design a dished-grid set in which all of
the beamlets emerge in a prescribed pattern. It is also important to
know when the grid set will experience an excessive accelerator impinge-
ment current and where over the dished grid surface the impingement is
occurring. Figure 28 shows perveance limit plots for the sample case
being considered. The allowed perveance profiles in this figure were
determined by computing the angular displacement between the thruster
centerline and the normal to the grid surface at each radial location
(θ in Fig. 22). For para-axial beamlets one wants $\beta = \theta$ so the re-
quired values of allowable deflection range are known. This information
is then used to enter the useful deflection range plots [(Fig. 12) for
$d_a/d_s = 1.00$ in this case] in this paper to determine the maximum per-
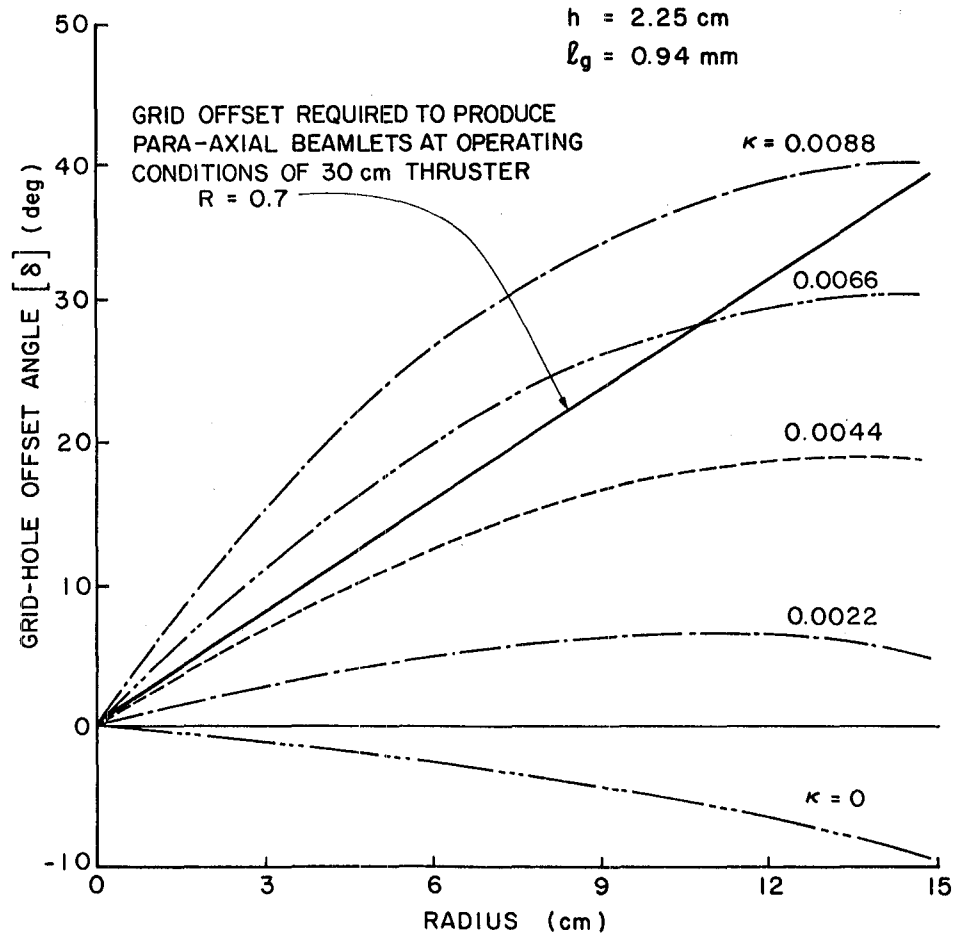veance allowed for a given deflection angle at each radial location
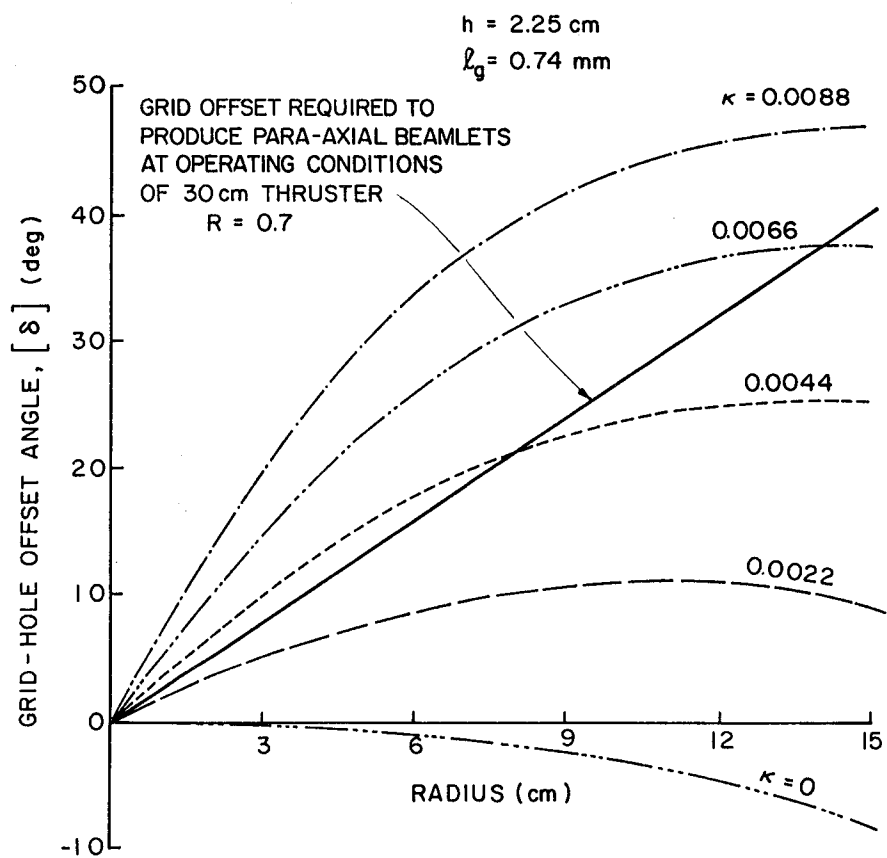
Figure 27. Dished Grid Offset Angles at Operating Temperatures for Various Accelerator Grid Compensations, Cold Dish Depth 2.25 cm, Cold Grid Separation Distance 0.74 mm
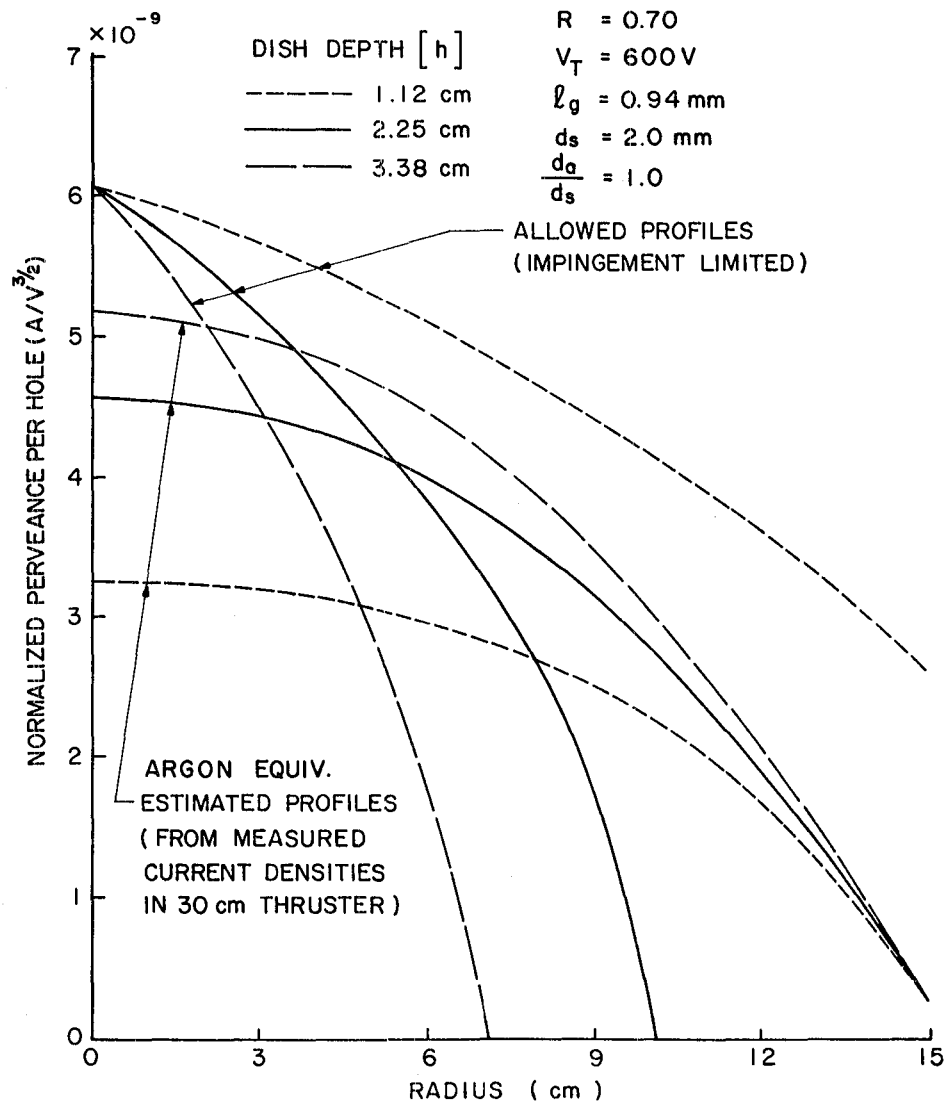
Figure 28. Typical Comparision of Allowed Perveance and Estimated
Perveance for 30 cm Dished Grids with Various Dish Depths

before direct accelerator grid impingement becomes excessive. The result is a plot of maximum perveance at each radial position for para-axial beamlets. It should be noted that for the larger dish depths these curves do not extend to the outer radius of the thruster, since the angle between the thruster axis and the normal to the grids at these points is greater than the maximum obtainable beamlet deflection angle at zero perveance. Also shown in Fig. 28 are the estimated perveance profiles that would be observed in the 30 cm thruster operating at the current per hole values of Fig. 23. These curves, each corresponding to a different dish depth, are shown because the thermal expansion of the grids results in different amounts of screen-accelerator grid hole offset for each dish depth. It can be seen from Fig. 28 that the allowed profile for the shallowest dish depth (h = 1.12 cm) is above the corresponding estimated profile at all radii. This indicates the impingement levels will be low over the entire accelerator grid surface in this case. For the greater dish depth curves, however, the allowed profiles fall below the estimated ones at the greater radii. In this case impingement would be expected to be more substantial. For the case under consideration the optimum dish depth seems to fall approximately midway between h = 2.25 cm and h = 1.12 cm. At zero radius, the estimated perveance profile drops with decreasing dish depth. This is due to the thermally induced decrease in separation gap which is a maximum at the center line and is more pronounced at small dish depths as previously seen in Fig. 26 (the screen grid is assumed to be hotter than the accelerator grid and therefore expands more). This problem could be alleviated somewhat by varying the initial grid separation as previously stated. A potential problem also exists for large diameter

multipole thrusters. In this type of thruster, the discharge chamber
design produces a much flatter plasma density profile across the
thruster radius. The thruster would then have a much flatter current
per hole profile than the one shown in Fig. 23 for a divergent field
thruster. As seen in Figs. 24 and 25, relatively large offset angles
may be required for the apertures at the outer edges of the grids in
large diameter thrusters. Because of the flatter current per hole
profiles in multipole thrusters, these outer radius holes may be ex-
pected to operate at higher perveance values. This would be expected
to create even more severe impingement problems if the beamlets are to
be re-directed parallel to the thruster axis than was observed in
Fig. 28 for the 30 cm divergent field thruster.

VI. CONCLUSIONS

Ion beamlet deflections of several degrees can be induced by displacing the screen and accelerator grid holes relative to each other. This deflection is limited to a useful range by the onset of high accelerator grid impingement currents. This range is primarily dependent on the perveance at which the beamlet is operating and the diameter of the accelerator grid aperture relative to the screen grid aperture diameter. The useful range is also dependent to a lesser extent on the net-to-total voltage ratio, grid separation distance, grid thicknesses, and the total accelerating voltage. Over the useful range of beam deflections the beamlet divergence angle is independent of deflection. In this range the deflection angle is also a linear function of the grid offset angle. The constant of proportionality between these angles exhibits a dependence on the net-to-total accelerating ratio but is relatively independent of the other parameters studied. Good agreement between the theoretical approximation and experimental results for this constant has been demonstrated.

The beamlet deflection data developed in this study can be used to design large diameter dished-grid accelerator systems in which the ion beamlets are to be directed along the thruster axis. In order to do this it is necessary to adjust the accelerator grid center-to-center hole spacing relative to the screen grid center-to-center hole spacing. The extent of the compensation required is determined primarily by the grid dish depth, the grid separation distance and the allowable

accelerator grid impingement current. The results would also be useful to an ion source designer who desires to control the direction of beamlets emitted from two grid optics by a relative grid translation.

Additional work concerning ion beamlet steering could be done to study the effects of higher total accelerating voltages on beamlet deflections. Also, future work should include a study of beamlet steering for three-grid optics. The addition of a third grid aperture, at ground potential, downstream of the accelerator grid results in improved beamlet focussing at low R-values.[14] An understanding of the beamlet steering characteristics of such a three-grid system would be useful for the design of ion thruster operating at these low R-values.

REFERENCES

1. Latham, W. C. and W. B. Adam, "Theoretical Analysis of a Grid Translation Beam Deflection System for a 30 cm Diameter Kaufman Thruster," NASA TM X-67911, 1971.

2. Kaufman, H. R., J. M. E. Harper, and J. J. Cuomo, "Focused Ion Beam Design for Sputter Deposition" Journal of Vac. Science & Tech., May/June 1979, pp. 899-905.

3. Aston, G., "The Ion-Optics of a Two-Grid Electron-Bombardment Thruster," NASA CR-135034, May 1976.

4. Aston, G., Kaufman, H. R. and Wilbur, P. J., "The Ion Beam Divergence Characteristics of Two-Grid Accelerator Systems," AIAA Journal, Vol. 16, No. 5, May 1971, pp. 516-524.

5. Kaufman, H. R., "Technology of Electron Bombardment Ion Thrusters." Advances in Electronics and Physics, Vol. 36, Academic Press Inc., San Francisco, 1974, pp. 289-291, 324-327, 330.

6. Whealton, J. H., "Linear Optics Theory of Ion Beamlet Steering," Rev. of Sci. Instrum., Vol. 48, No. 11, 1977, pp. 1428-1429.

7. Spangenberg, K. R., Vacuum Tubes, McGraw Hill, New York, 1948, pp. 97-111, 328-355.

8. Stewart, L. D., Kim, J., and Matsuda, S., "Beam Focusing by Aperture Displacement in Multi-ampere Ion Sources," Rev. Sci. Instrum., Vol. 46, No. 9, Sept. 1975, pp. 1193-1196.

9. Wilbur, P. J., Advanced Space Propulsion Thruster Research, NASA CR-165584, pp. 127-130.

10. Aston, G., "Ion Extraction from a Plasma," NASA CR-159849, June 1980, pp. 35-39.

11. Poeschel, R. L., et. al., "High Power and 2.5 kw Advanced Technology Ion Thrusters," NASA CR-135163, 1977, p. 34.

12. Rawlin, V. K., Banks, B. A., and Byers, D. C., "Design, Fabrication, and Operation of Dished Accelerator Grids on a 30-cm Ion Thruster," NASA TM X-68013, 1972.

13. Rawlin, V. K., Banks, B. A., and Byers, D. C., "Dished Accelerator Grids on a 30-cm Ion Thruster," Journal of Spacecraft and Rockets, Vol. 10, No. 1, Jan., 1973, pp. 29-35.

14. Aston, G. and Kaufman, H. R., "Ion Beam Divergence Characteristics of Three-Grid Accelerator Systems," AIAA Paper No. 78-669, 13th International Electric Propulsion Conference, April 1978.

APPENDIX A

Acceleration Length Definition

Previous researchers[2,3,4] have used an effective acceleration length defined by:

$$\ell_e = [\ell_g^2 + \frac{d_s^2}{4}]^{\frac{1}{2}} \; . \qquad (A-1)$$

This definition assumes the plasma sheath is located close to the downstream edge of the screen grid hole. Subsequent studies[10] have shown that the discharge chamber plasma never enters the screen hole under normal operating conditions. Therefore, an effective acceleration length which includes the screen grid thickness is possibly a better approximation to the true acceleration length. In this study the effective acceleration length has been defined as:

$$\ell_e' = [(\ell_g + t_s)^2 + \frac{d_s^2}{4}]^{\frac{1}{2}} \; . \qquad (A-2)$$

A comparison of Eqs. A-1 and A-2 shows that the difference in effective acceleration length becomes more pronounced for grids in which t_s/d_s begins to approach ℓ_g/d_s.

The effect of computing the normalized perveance per hole in terms of the length ℓ_e' rather than ℓ_e is illustrated comparatively for the standard grid set in Fig. A-1. The result is a change in the perveance scale alone, the positions of the data points relative to one another are unchanged. This scale can be applied to all of the data plots

ARGON

$V_T = 600$ V

$\dfrac{\ell_g}{d_s} = 0.49$

$\dfrac{d_a}{d_s} = 0.64$

$\dfrac{t_a}{d_s} = 0.37$

$\dfrac{t_s}{d_s} = 0.18$

$R = 0.70$
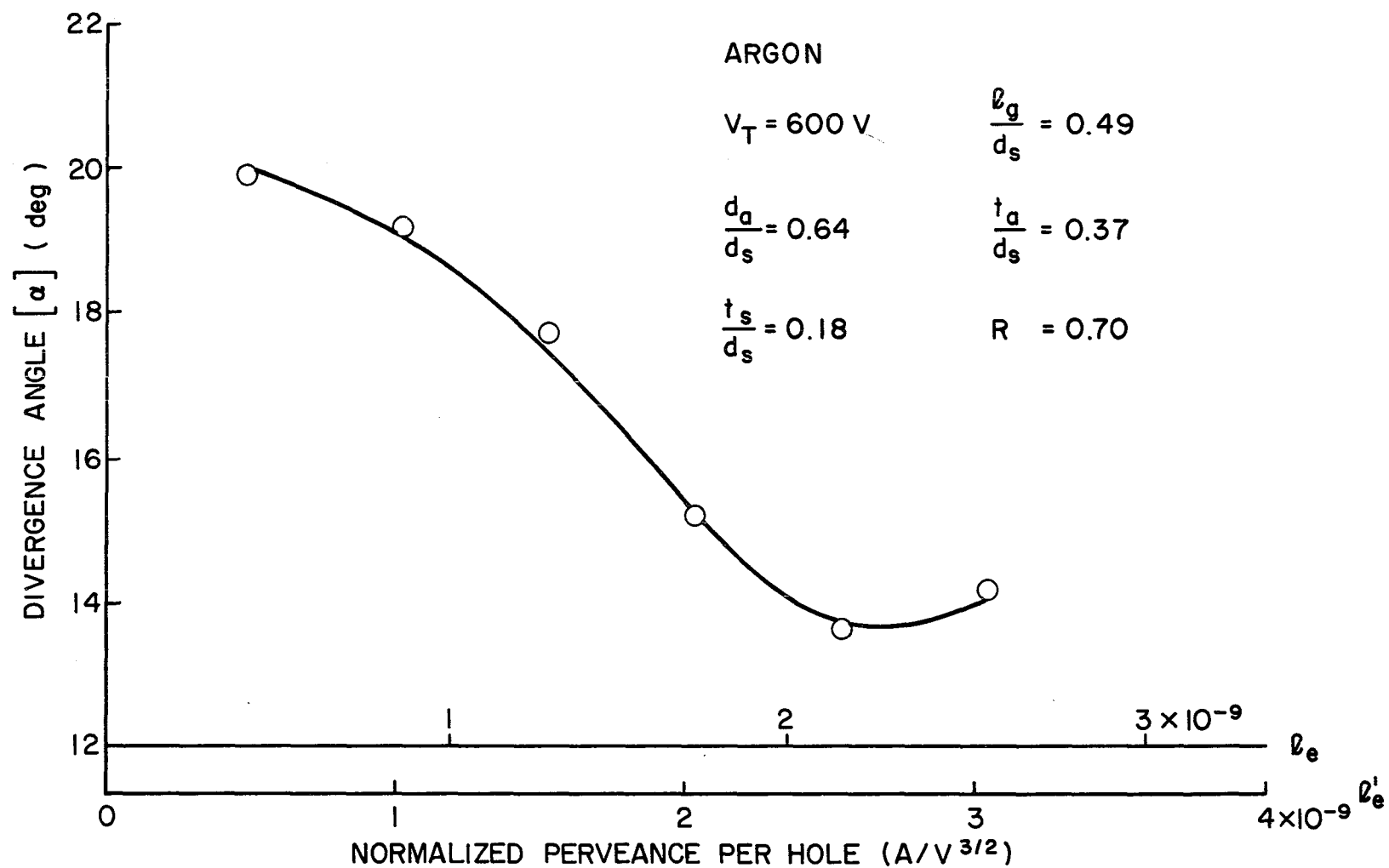
Figure A-1   Comparison of Normalized Perveance per Hole Scales for Acceleration Lengths ℓ_e and ℓ_e' , Standard Grid Set Divergence Angle Results

appearing in Section IV as a function of normalized perveance per hole, with the exception of those plots which vary the terms included in the effective acceleration length definition (screen grid thickness and grid separation distance).

The data points for variations of screen grid thickness and grid separation distance have been re-plotted with respect to the standard case geometry in Figs. A-2 and A-3. The only significant change is for the case of a thick screen grid. The overall effect of the change in perveance scale was to place the data points at lower values of perveance when the screen grid thickness was not incorporated into the definition of acceleration length.
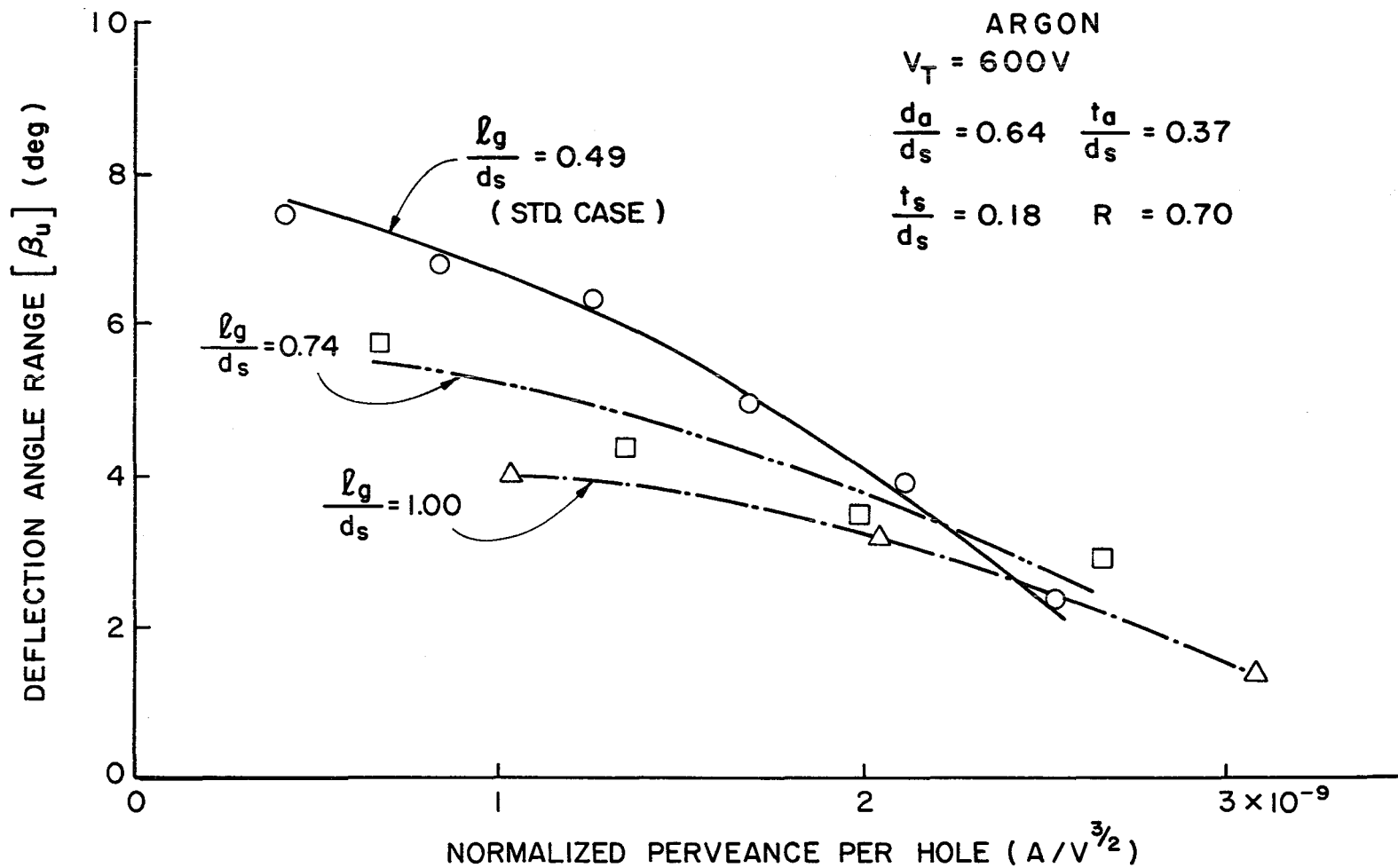
Figure A-2   Deflection Angle Range for Various Grid Separation Ratios,
NP/H with Acceleration Length ℓ_e

DEFLECTION ANGLE RANGE $[\beta_u]$ (deg)

NORMALIZED PERVEANCE PER HOLE ($A/V^{3/2}$)

ARGON
$V_T = 600V$

$\dfrac{\ell_g}{d_s} = 0.49$ $\dfrac{t_a}{d_s} = 0.37$

$\dfrac{d_a}{d_s} = 0.64$ $R = 0.70$

$\dfrac{t_s}{d_s} = 0.18$

(STD. CASE)

$\dfrac{t_s}{d_s} = 0.37$

10

8

6

4

2

0

0

1

2

3×10^{-9}

70
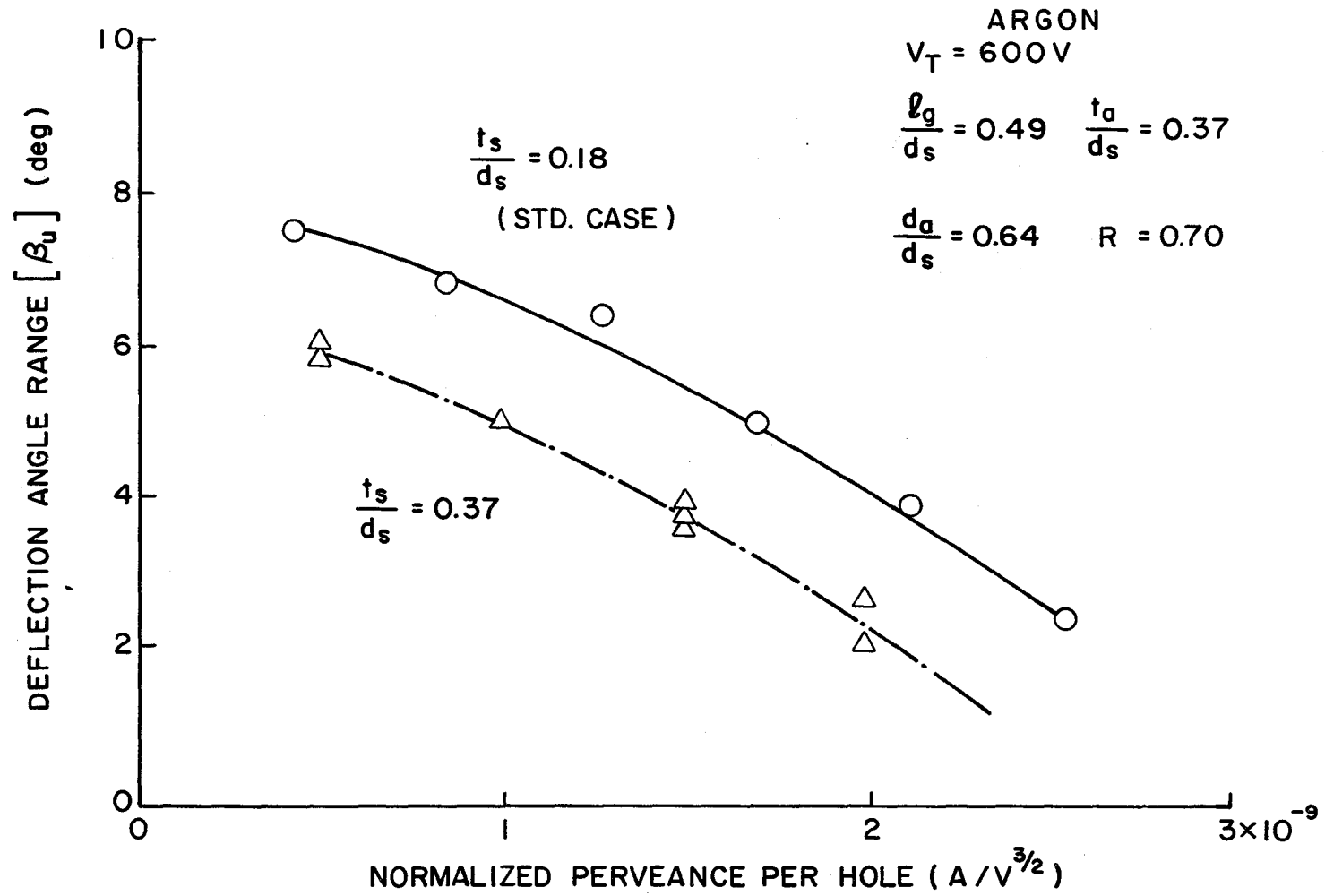
Figure A-3   Deflection Angle Range for Various Screen Grid Thickness Ratios,
NP/H with Acceleration Length ℓ_e

APPENDIX B

Experimental Results

$\dfrac{d_a}{d_s}$	$\dfrac{\ell_g}{d_s}$	$\dfrac{t_s}{d_s}$	$\dfrac{t_a}{d_s}$	$\dfrac{V_N}{V_T}$	V_T (v)	NP/H Nanopervs/ hole	β/δ	β_u (deg)	α (deg)
0.64	0.49	0.18	0.37	0.70	600	0.51	0.443	7.5°	19.9°
						1.02	0.425	6.8	19.2
						1.53	0.452	6.0	18.1
						2.04	0.450	5.0	15.2
						2.55	0.483	3.9	13.6
						3.06	0.312	2.4	14.1
				0.50		0.51	0.455	7.6	22.8
						1.02	0.465	7.1	21.7
						1.53	0.506	6.2	20.9
						2.04	0.515	5.9	19.8
						2.55	0.558	5.4	17.8
						3.06	0.409	3.4	16.9
				0.90		0.51	0.398	7.0	18.2
						1.02	0.409	5.8	17.1
						1.53	0.409	5.4	15.5
						2.04	0.397	4.3	12.9
						2.55	0.402	3.5	12.4
						3.06	0.414	2.8	11.2
0.83	0.49	0.18	0.37	0.70	600	0.51	0.395	8.2	20.2

$\dfrac{d_a}{d_s}$	$\dfrac{\ell_g}{d_s}$	$\dfrac{t_s}{d_s}$	$\dfrac{t_a}{d_s}$	$\dfrac{V_N}{V_T}$	V_T (v)	NP/H Nanopervs/hole	β/δ	β_u (deg)	α (deg)
0.83	0.49	0.18	0.37	0.70	600	1.02	0.360	7.7°	19.6°
						1.53	0.417	7.5	17.9
						2.04	0.402	7.3	17.0
						2.55	0.406	6.9	15.4
						3.06	0.489	6.2	15.7
						3.56	0.509	5.6	16.1
				0.50		0.51	0.435	9.0	22.3
						1.02	0.459	9.0	20.4
						1.53	0.503	8.4	20.6
						2.04	0.463	8.1	19.2
						2.55	0.467	7.8	18.0
						3.06	0.556	7.3	18.1
				0.90		0.51	0.359	7.5	18.8
						1.02	0.346	7.3	18.1
						1.53	0.352	6.7	16.3
						2.04	0.406	6.4	14.3
						2.55	0.366	5.5	14.6
						3.06	0.413	5.3	14.0
1.00	0.49	0.18	0.37	0.70	600	0.51	0.432	11.8	19.1
						1.02	0.443	11.3	18.1
						1.53	0.457	11.2	16.4
						2.04	0.464	10.7	15.0
						2.55	0.452	10.1	14.8
						3.06	0.454	9.3	14.6
						3.56	0.422	7.6	13.4

$\dfrac{d_a}{d_s}$	$\dfrac{\ell_g}{d_s}$	$\dfrac{t_s}{d_s}$	$\dfrac{t_a}{d_s}$	$\dfrac{V_N}{V_T}$	V_T (v)	NP/H Nanopervs/ hole	β/δ	β_u (deg)	α (deg)
1.00	0.49	0.18	0.37	0.50	600	0.51	0.432	11.8°	21.8°
						1.02	0.457	12.2	20.6
						1.53	0.469	12.1	19.0
						2.04	0.493	11.4	17.5
						2.55	0.523	10.9	17.3
						3.06	0.524	10.4	17.1
						3.56	0.518	8.9	16.9
				0.90		0.51	0.386	10.7	16.9
						1.02	0.383	10.4	15.5
						1.53	0.370	9.3	13.2
						2.04	0.376	9.1	12.0
						2.55	0.380	8.4	11.6
						3.06	0.385	7.8	12.6
						3.56	0.346	6.7	12.7
0.64	0.74	0.18	0.37	0.70	600	0.79	0.443	5.6	16.2
						1.59	0.462	4.4	15.1
						2.38	0.439	3.5	13.5
						3.17	0.543	2.9	13.0
				0.50		0.79	0.506	6.2	19.5
						1.59	0.514	5.0	18.6
						2.38	0.583	4.0	17.4
						3.17	0.612	2.6	13.7
				0.90		0.79	0.476	6.4	15.0
						1.59	0.406	4.0	12.8
						2.38	0.400	2.9	10.8

$\dfrac{d_a}{d_s}$	$\dfrac{\ell_g}{d_s}$	$\dfrac{t_s}{d_s}$	$\dfrac{t_a}{d_s}$	$\dfrac{V_N}{V_T}$	V_T (v)	NP/H Nanopervs/ hole	β/δ	β_u (deg)	α (deg)
0.64	0.74	0.18	0.37	0.90	600	3.17	0.421	1.3°	10.1°
0.64	1.00	0.18	0.37	0.70	600	1.18	0.446	4.2	13.0
						2.37	0.440	3.2	11.7
						3.55	0.471	1.4	9.8
				0.50		1.18	0.550	4.8	16.8
						2.37	0.612	3.5	14.2
						3.55	0.555	1.8	13.1
				0.90		1.18	0.400	3.6	12.0
						2.37	0.398	2.6	7.9
						3.55	0.399	1.3	6.8
0.64	0.49	0.37	0.37	0.70	600	0.71	0.498	5.9	18.0
						1.43	0.504	5.0	17.3
						2.14	0.505	3.8	15.1
						2.86	0.525	2.4	12.8
				0.50		0.71	0.643	6.9	22.3
						2.14	0.594	4.5	19.7
				0.90		0.71	0.488	5.5	16.3
						2.14	0.475	3.5	13.1
0.64	0.49	0.18	0.12	0.70	600	0.51	0.540	8.0	21.0
						1.02	0.518	6.7	20.3
						1.53	0.425	6.0	19.4
						2.04	0.446	5.5	17.2
						2.55	0.503	5.0	15.7
				0.50		0.51	0.593	9.0	24.7
						1.02	0.469	8.2	23.8

$\dfrac{d_a}{d_s}$	$\dfrac{\ell_g}{d_s}$	$\dfrac{t_s}{d_s}$	$\dfrac{t_a}{d_s}$	$\dfrac{V_N}{V_T}$	V_T (v)	NP/H Nanopervs/ hole	β/δ	β_u (deg)	α (deg)
0.64	0.49	0.18	0.12	0.50	600	1.53	0.607	7.2°	22.5°
						2.04	0.538	6.4	20.6
						2.55	0.574	6.0	17.8
				0.90		0.51	0.480	7.2	19.5
						1.02	0.430	6.1	18.4
						1.53	0.408	5.2	15.8
						2.04	0.409	4.7	13.9
						2.55	0.487	4.1	12.7
0.64	0.49	0.18	0.74	0.70	600	0.51	0.444	5.0	20.9
						1.02	0.516	5.2	20.6
						1.53	0.464	4.7	19.4
						2.04	0.555	3.3	17.5
						2.55	0.452	3.3	16.4
						3.06	0.420	2.8	16.3
				0.50		0.51	0.459	4.9	24.6
						1.53	0.556	5.5	22.7
						2.55	0.572	2.8	19.9
				0.90		0.51	0.393	4.3	19.0
						1.53	0.439	4.2	16.0
						2.55	0.392	2.6	13.3
0.64	0.49	0.18	0.37	0.70	1100	0.21	0.370	6.5	24.2
						0.62	0.417	7.8	23.0
						1.03	0.442	8.0	23.2
						1.44	0.512	7.4	21.7
						1.64	0.491	7.5	21.5

$\dfrac{d_a}{d_s}$	$\dfrac{\ell_g}{d_s}$	$\dfrac{t_s}{d_s}$	$\dfrac{t_a}{d_s}$	$\dfrac{V_N}{V_T}$	V_T (v)	NP/H Nanopervs/ hole	β/δ	β_u (deg)	α (deg)
0.64	0.49	0.18	0.37	0.70	1100	2.06	0.522	6.8°	19.2°
						2.47	0.534	5.8	18.0
						2.67	0.563	6.4	17.6
				0.50		0.62	0.469	7.5	25.8
						1.03	0.462	8.9	24.9
				0.90		0.62	0.377	6.9	21.4
						1.03	0.379	6.7	20.6
0.64	0.49	0.18	0.37	0.35	600	0.51	0.578	7.7	26.8
						1.02	0.586	6.8	24.6
						1.53	0.654	5.7	24.1
						2.04	0.633	3.4	20.7

End of Document